NATIONAL AERONAUTICS AND SPACE ADMINISTRATION

## Technical Report 32-1562

# Summary Report on the Development, Design and Test of a 66-W/kg (30-W/lb) Roll-Up Solar Array

W. A. Hasbach
R. G. Ross, Jr.

JET PROPULSION LABORATORY
CALIFORNIA INSTITUTE OF TECHNOLOGY
PASADENA, CALIFORNIA

September 15, 1972

NATIONAL AERONAUTICS AND SPACE ADMINISTRATION

## *Technical Report 32-1562*

# *Summary Report on the Development, Design and Test of a 66-W/kg (30-W/lb) Roll-Up Solar Array*

*W. A. Hasbach*
*R. G. Ross, Jr.*

**JET PROPULSION LABORATORY**
**CALIFORNIA INSTITUTE OF TECHNOLOGY**
**PASADENA, CALIFORNIA**

September 15, 1972

# Preface

The work described in this report was performed by the General Electric Co. under the cognizance of the Guidance and Control Division of the Jet Propulsion Laboratory.

# Contents

# Contents (contd)

## Tables

## Figures

# Contents (contd)

## Figures (contd)

# Abstract

This report summarizes the results of a program to develop a 23-m$^2$ (250-ft$^2$) roll-up solar array with a power-to-weight ratio exceeding 66 W/kg (30 W/lb). Descriptions of the system design and fabrication of a full-scale engineering development unit are included, the system and development test program results are described, and conclusions are drawn. Special test equipment and test procedures are included, together with comparisons of experimental and analytical results.

# Summary Report on the Development, Design and Test of a 66-W/kg (30-W/lb) Roll-Up Solar Array

## I. Introduction

This report contains a summary of the work performed under JPL Contract 952314, Design and Development of a 66-W/kg (30-W/lb), 23-m$^2$ (250-ft$^2$) roll-up solar array, by the General Electric Co., Space Systems Organization, Valley Forge, Pennsylvania. The program objective was to develop the technology of the roll-up solar array concept by preparing a detailed design, performing the associated analyses, fabricating an engineering model, and subjecting the engineering model to a comprehensive test program consisting of both environmental and development tests. The design concept was based on the results of the feasibility study described in Ref. 1. The goals of the program were to advance the state-of-the-art of solar arrays for future space missions requiring increased capability in terms of weight and stowed volume relative to that provided by current rigid-panel concepts. The model spacecraft used as a baseline for the feasibility study was an interplanetary vehicle oriented with respect to the sun. However, the vehicle concept was for reference only, and the array design was intended to be adaptable to a variety of vehicle configurations and missions. Weight was a primary consideration in all design decisions.

The configuration developed in the feasibility study, fabricated and tested in this program, is shown in Fig. 1. A general description of the array configuration is included in Section II, along with detailed descriptions of the array components and construction details. Sections III and IV summarize the weight breakdown and electrical performance of the array.

Because of the flexible nature of the deployed array and the possibility of adverse interaction with spacecraft attitude control systems, a significant effort was devoted to analyzing and measuring the deployed dynamics of the array. The actual test program was conducted in two parts. The first series of tests and analyses were conducted immediately following the completion of the array fabrication and concentrated on the out-of-plane modal characteristics of the deployed array. The results of this sequence of tests are described and compared with analytical predictions in Section V.

Although in-plane mode measurements were conducted in the first modal test sequence, large discrepancies were noted in both the modal test and analytical results for this mode. These discrepancies were caused by the highly nonlinear and very complex in-plane structural behavior of the array. To gain an understanding of this behavior, an additional combined analytical and experimental program was conducted. The results of this in-plane dynamic analysis effort are described in Section VI.

In the program sequence, the deployed modal tests were followed by a rigorous environmental test program consisting of pyrotechnic shock, thermal vacuum, acoustic noise, and stowed vibration tests. The array successfully survived these tests, and only small differences between predicted and measured response characteristics were noted. These tests and their results are discussed in Section VII. The effect of the test sequence on the system electrical and mechanical performance is summarized in Section VIII.

During the contract period, a number of development tests were also performed to evaluate the mechanical and thermal-mechanical properties of various array components. These tests explored bi-stem thermal and static load deflection characteristics, solar cell module thermal-cycling and bending stiffness characteristics, and blanket tracking characteristics. The results of these tests are discussed in Section IX, along with the results of a supplemental test to determine the relationship between blanket wrap tension and blanket slack formation during stowed vibration.

The final section, Section X, contains a list of conclusions derived from the program and identifies areas in which particularly significant results have been obtained and a few areas in which further work could lead to even lighter-weight designs.

Where units of measurement are given in both the metric and the English system, the actual measurements were made in English units.

## II. Description of the System

The roll up solar array which was designed, fabricated and tested during this program provides 23 m² (250 ft²) of deployed solar cell module area. The solar cells are mounted on two 1.2 × 10.2 m (3.8 × 33.5 ft) flexible substrates of Kapton-H film, which are stored on drums during launch. The configuration is shown in Fig. 1. Each drum is cantilevered from a center support structure on a bearing system and has a slip-ring assembly for the transfer of power and signals, and a Negator spring motor that provides a constant tension in the deployed solar array blanket. A deployable boom is mounted on the center support and is attached to a leading-edge member which supports the outer end of the solar cell blankets. Outboard end supports support the outboard drum ends only during launch and are pyrotechnically released before the system is de-

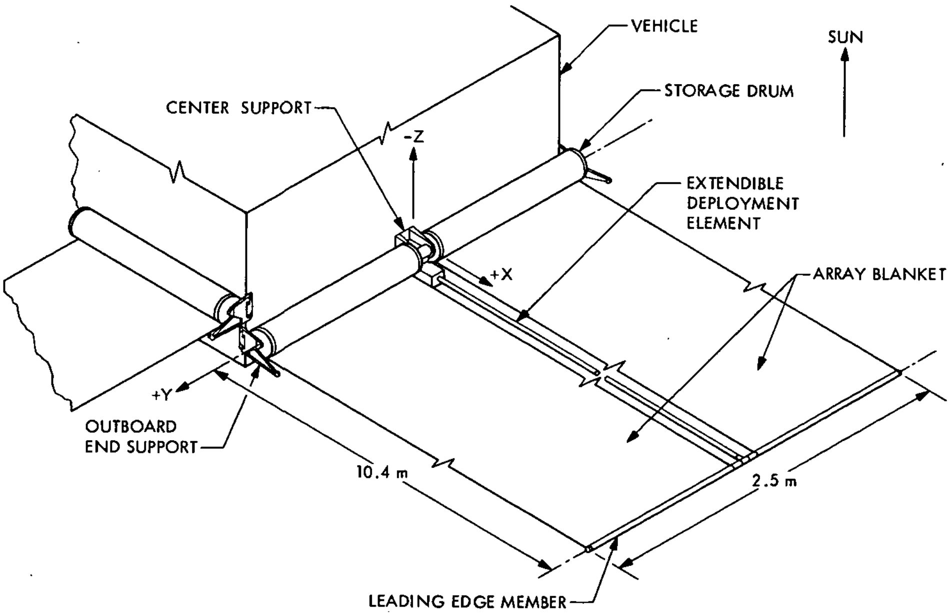

**Fig. 1. Roll-up solar array configuration (coordinate system shown)**

ployed by extending the boom. Figure 2 pictures the model in both stowed and fully deployed states.

The seven major elements which make up the solar array system are described in the following subsections. Detailed descriptions and drawings are included in Ref. 2.

## A. Array Blankets

The array consists of two blankets, each 1.17 m (46-in.) wide × 10.21 m (402 in.) long, with end leaders extending beyond the cells at both ends. A blanket supports six circuits, each of which consists of 242 cells in series by 19 cells in parallel. These circuits are bonded to a 0.005-cm (0.002-in.) Kapton-H film substrate, which is fabricated from copper-clad Schjel-Clad L-7510 by etching out the unwanted copper, leaving the conductor bus strip system. Each circuit feeds into the main positive and negative bus, which in turn connects to the power feedthrough at the drum. All connections from the cell side of the substrate to the bus strip system on the backside are made around the edges rather than through holes in the substrate. These connections are also made with Schjel-Clad L-7510, which is bonded to the Kapton substrate with SMRD-745[*] adhesive and soldered to the solar cell modules on the front and the bus strips on the rear. The exposed copper bus strips on the rear of the substrate are covered with Kapton silicone adhesive pressure-sensitive tape. Foamed RTV 560 cushioning buttons were applied to the backside of the substrate at the corners of each solar cell. These buttons supply interlayer cushioning in the stowed configuration. For economic reasons, the engineering test model was fabricated with partial solar cell coverage. The remaining area was covered with dummy glass modules fabricated from 0.028 × 2 × 2 cm (0.011 × 0.75 × 0.75 in.) pieces of Corning 0211 microsheet joined together with strips of 0.635-cm (¼-in.) wide Kapton silicone adhesive pressure-sensitive tape. The glass platelet modules provided an accurate mass simulation of the solar cell modules, and the tape simulated the bending stiffness of the actual solar cell interconnections.

In order to incorporate a representative sampling of various interconnection approaches, several recognized solar array fabricators were invited to supply sample modules fabricated with established production techniques. Table 1 lists these modules, along with the overall dimensions in the series and parallel direction. The weight of the modules reflects the basic differences in

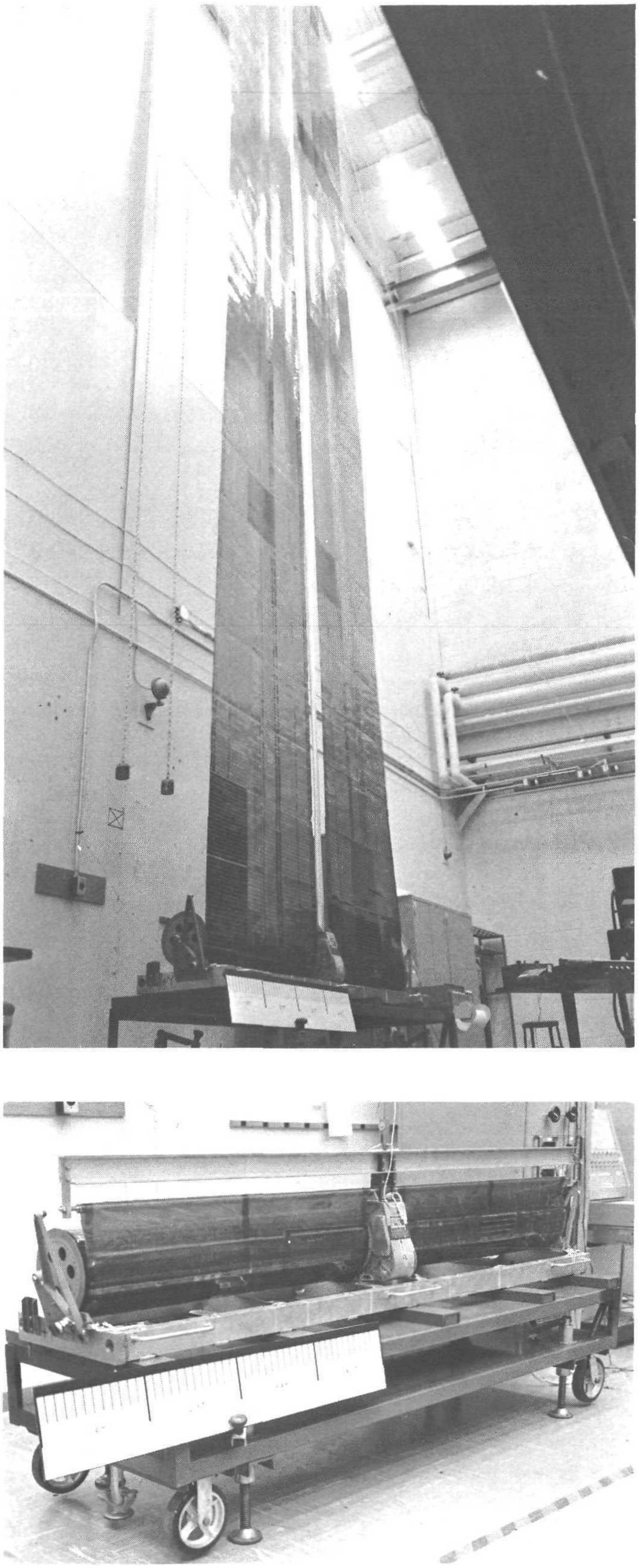

Fig. 2. Prototype test model: (a) deployed, (b) stowed

---

[*] SMRD-745 is a flexible epoxy formulated by General Electric Co. Space Systems. It is available from Space Systems on a special-order basis.

Table 1. Solar cell module summary

| Module designation | Size | Dimension series direction, m | Dimension parallel direction, m | Module weight, g | Weight per cell, g | Total array weight differential,[a] kg | Interconnect material |
|---|---|---|---|---|---|---|---|
| GE No. 1 | 19p × 20s | 0.4135 | 0.3853 | 112.5 | 0.2961 | +0.222 | Ag-expanded metal, 0.005 cm thick |
| GE No. 2 | 19p × 20s | 0.4140 | 0.3853 | 108.5 | 0.2855 | −0.165 | |
| GE No. 3 | 19p × 20s | 0.4127 | 0.3865 | 113.5 | 0.2987 | +0.363 | |
| Heliotek | 19p × 20s | 0.4147 | 0.3870 | 135.5 | 0.3566 | +3.561 | Cu, 1/2 hard, 0.005 cm thick |
| Spectrolab | 12p × 20s | 0.4142 | 0.2446 | 81.0 | 0.3375 | +2.504 | Cu, 1/2 hard, 0.005 cm thick |
| Boeing | 18p × 20s | 0.4099 | 0.3698 | 99.5 | 0.2764 | −0.866 | Ag-expanded metal |
| EOS | 18p × 20s | 0.4150 | 0.3695 | 122.8 | 0.3411 | +2.703 | Kovar |
| Centralab No. 1 | 19p × 20s | 0.4206 | 0.3873 | 121.0 | 0.3184 | +1.451 | Kovar-expanded metal, 0.002 cm thick |
| Centralab No. 2 | 19p × 20s | | | | | | |
| Centralab No. 3 | 19p × 20s | | | | | | |
| Centralab No. 4 | 19p × 20s | | | | | | |

[a] Total array weight increase (or decrease) if this module configuration were used on the flight array (based on 19 parallel × 20 series module weight of 111 g).

the interconnect design. The weight differential column represents the total weight difference if that particular module configuration were used for a flight array (based on a 19 parallel × 20 series module weight of 111 g). These modules were bonded to the substrates with SMRD-745. Figure 3 shows a completed blanket before attachment to the storage drum. The two main bus strips at the drum end of the blanket are visible through the Kapton-H film substrate.

### B. Solar Panel Actuator

The solar panel actuator is a bi-stem deployable boom, designed and developed by SPAR Aerospace Products, Ltd. Figure 4 shows this component mounted on the center support structure between the drums. The boom element of the bi-stem unit forms the primary structure in the deployed configuration and has a diameter of 3.403 cm (1.34 in.). It is made of two 301 stainless steel strips, 10.16 cm (4 in.) wide and 0.0178 cm (0.007 in.) thick, which are pre-stressed to form an overlapped tube in the deployed position. The boom is silver-plated on its outside surface to reduce the temperature gradients in the boom when one side is exposed to solar radiation and the other side is in the shadow. Typical properties of the boom element are:

| | |
|---|---|
| Mass per unit length | 0.29 kg/m |
| Bending stiffness (EI) | 910 N-m$^2$ |
| Self-extension force | 54 N |

The solar panel actuator was subjected to component-level sinusoidal vibration tests before installation into the roll-up array system.

### C. Slip-Ring Assembly

The slip-ring assembly was designed and fabricated by Poly-Scientific Division of Litton Precision Products, Inc. A photograph of this component is shown in Fig. 5, and the pertinent design data are summarized in Table 2. Each storage drum contains a slip-ring assembly to transfer the array power and signals across the rotary joint between the drums and the center support. The storage drums rotate approximately 15 turns to deploy or retract the array.

### D. Storage Drum

The two storage drums in the system form the primary structure for the stowed configuration. Each drum assembly includes a shell, outboard end cap, inboard end cap, and edge guides. Two different drum configurations were designed for this application: one utilizing a beryllium monocoque shell, and the other fabricated with a magnesium semi-monocoque shell. For economic reasons, the magnesium shell design was selected for use on the test model, even though a total weight penalty of 0.9 kg (2 lb) was incurred.

The drum shells are 1.196-m (47.1-in.) long, 0.081-cm (0.032-in.) thick sheet magnesium rolled into an 20.32-cm (8-in.) diameter cylinder, which is closed with a lap-butt joint utilizing a 1.9-cm (0.75-in.) wide strip of magnesium bonded with Epon 934.

The inboard end cap assembly, pictured in Fig. 6, houses the two main bearings, which allow the storage drum to rotate with respect to the support shaft. The constant-torque Negator spring motor, which provides the blanket preload force, is mounted with the output spool coaxial with the main bearings. The slip-ring assembly is then mounted to the outboard end of this output spool. The brushes of the slip-ring assembly are wired to the drum shell power feedthrough as shown. The outboard end cap serves as the supporting interface for the drum outer end during launch, and contains a tapered hole which mates with a tapered plug in the outboard end support.

Two edge guide flanges are mounted on each storage drum to provide control forces to the blanket edge during retraction. If, for any reason, the blanket should tend to rewrap against either flange, that guide will apply corrective forces to prevent the blanket from extending past the end of the drum.

## E. Leading Edge Member

The leading edge member (LEM) is the structural element at the outermost end of the blanket. In the deployed configuration, this member transmits the 18-N (4-lb) blanket preload force from the array substrates to the boom. In the stowed configuration, its function is to restrain the outer blanket wrap. The ends of the LEM are supported by the outboard end supports, and the center section is supported from the actuator housing by two saddle-type brackets. Located in the center of the member is a fitting that houses two instrument bearings which mate with the stainless steel boom post. These bearings decouple the array blanket from the bi-stem boom for rotation about the boom axis. With the exception of the stainless steel boom post, bearings, and associated spacers, all parts are made of beryllium.

## F. Outboard End Supports

During launch, the drums and leading edge member are supported by two outboard end supports, which are released after launch to permit deployment of the array. Each support consists of a movable arm assembly, as pictured in Fig. 7, on which are mounted two stainless steel tapered plugs that interface with the outboard end cap and LEM. Attachment of the movable arm to the spacecraft is through a hinge joint. A torsion spring which mounts on the hinge pin furnishes 11.3 m-N (100 in.-lb) torque in the stowed configuration. The release of the supports is accomplished by a separation nut/separation bolt/bolt catcher combination on each support. Torsion springs force the movable arms to rotate about their hinge pins through an angle of approximately 10 deg. The storage drum and the LEM are thus released to permit deployment by the bi-stem actuator.

**Table 2. Slip-ring data**

| Element description | Design data |
|---|---|
| Power rings per assembly | 2 |
| Signal rings per assembly | 4 |
| Structural material | 303 stainless steel |
| Ring material | Coin silver |
| Ring diameter | 1.52 cm |
| Brushes per signal ring | 2 |
| Brushes per power ring | 4 |
| Brush material | Silver/copper/niobium diselenide/graphite |
| Brush spring material | Ney Paliney 7 |
| Rated current per ring | |
| Power | 15 A dc |
| Signal | 1 A dc |
| Brush contact force | |
| Power | 1.5 N ± 10% |
| Signal | 0.5 N ± 10% |
| Starting torque | |
| Air | 8 N-cm |
| Vacuum | 4.5 N-cm |
| Signal ring static contact resistance | 0.065 Ω |
| Power ring static contact resistance | 0.02 Ω |
| Rated current density/ring | |
| Power | 29.1 A/cm$^2$ |
| Signal | 12.8 A/cm$^2$ |
| Anticipated power loss/assembly | 6 W |
| Weight/assembly | 0.28 kg |

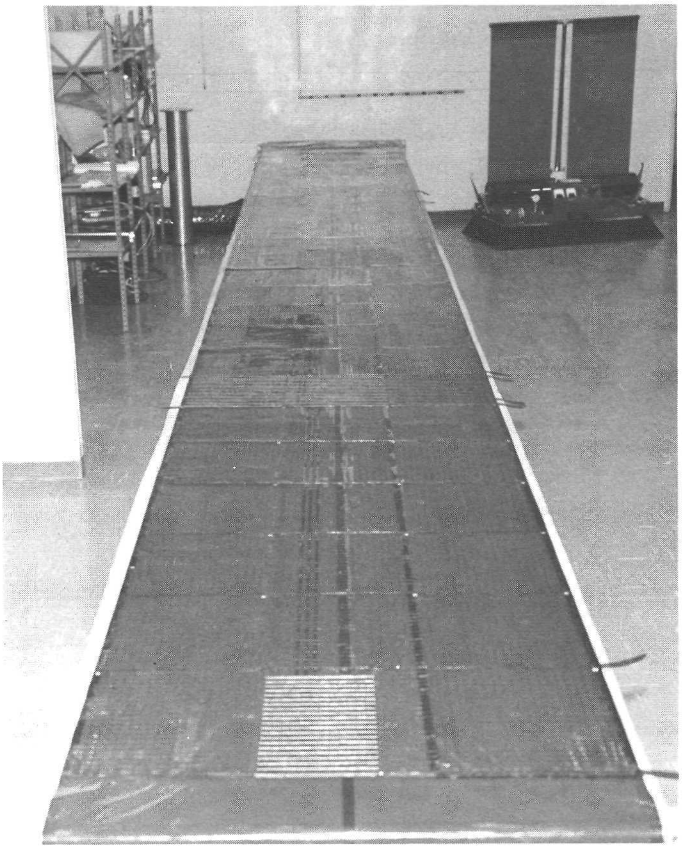

Fig. 3. −Y array blanket

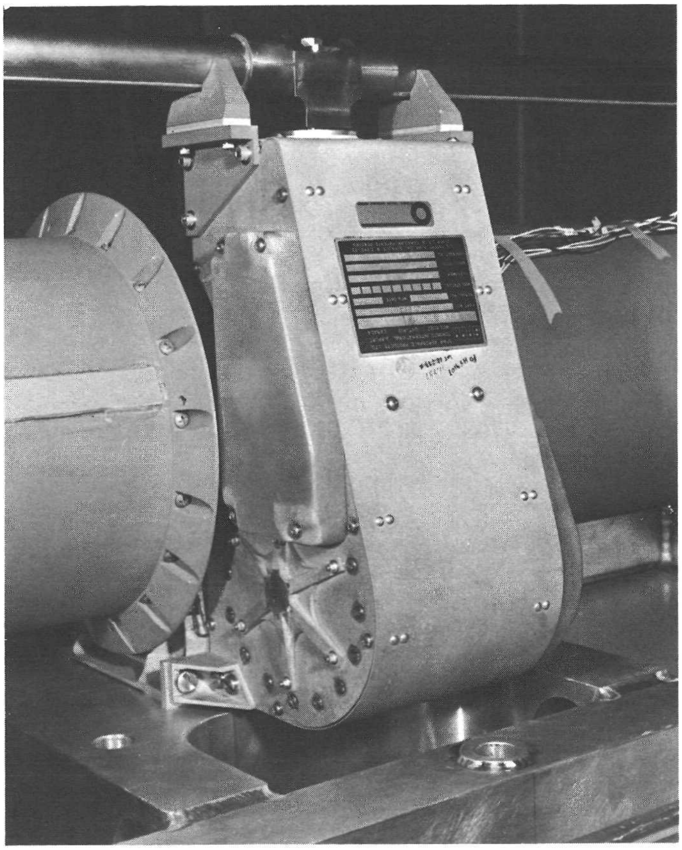

Fig. 4. Solar panel actuator

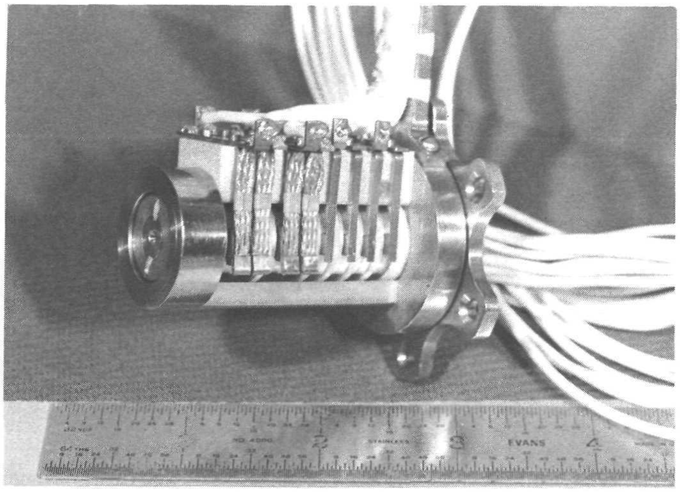

Fig. 5. Slip-ring assembly

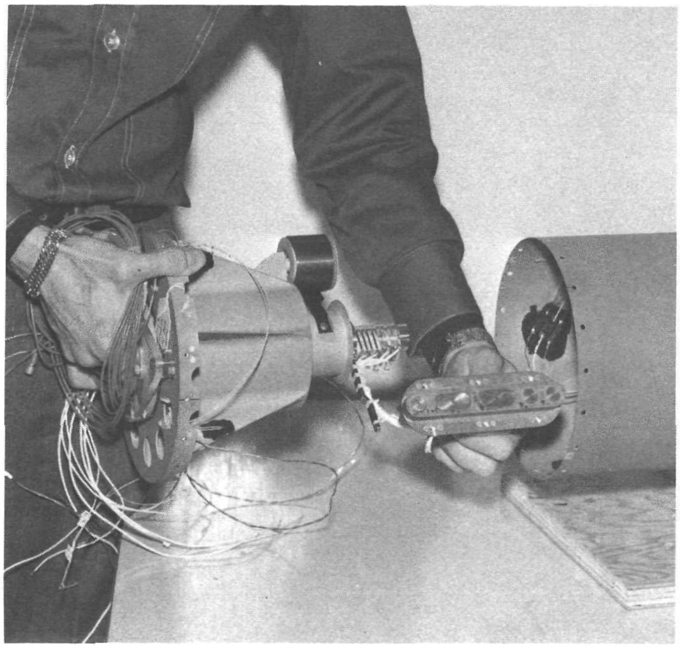

Fig. 6. Inboard end cap assembly

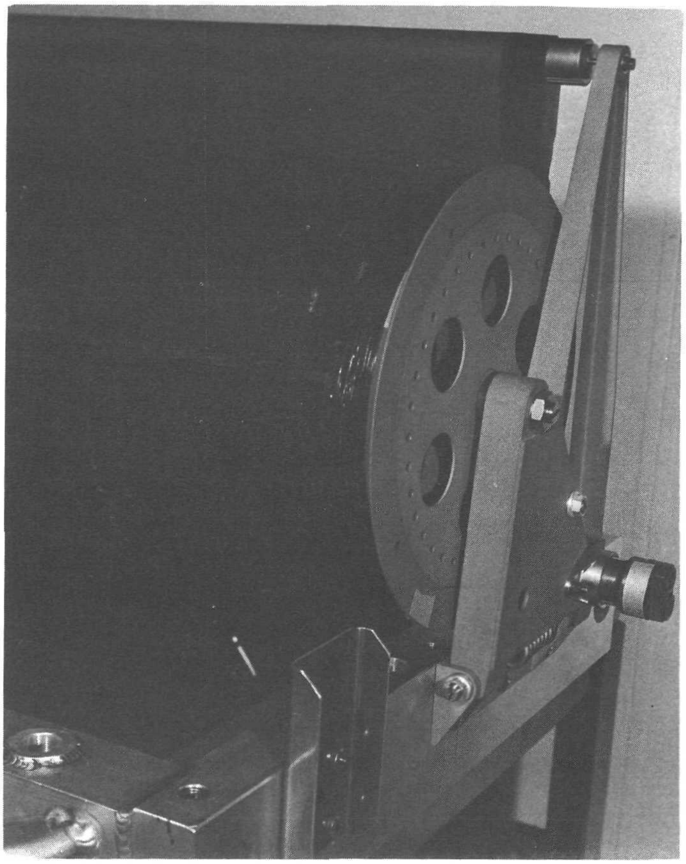

Fig. 7. Outboard end support

### G. Center Support

The center support consists of a magnesium center tube, two machined magnesium end fittings, and two magnesium face sheets. As shown in Fig. 8a, the center tube is pinned to the end fittings, and the face sheets are riveted to the tube end fittings. One face sheet provides for the electrical connector installation, and, together with the other face sheet, transmits shearloads. The end fittings provide the interface pads for the vehicle structure and the solar panel actuator. The five connectors shown in Fig. 8b carry the array power from the slip rings to the spacecraft.

## III. Mass Properties Summary

The weight breakdown for the engineering model is shown in Table 3. The total weight of this model is 37.4 kg (82.5 lb). Based on this weight, the array power-to-weight ratio is 67 W/kg (30.3 W/lb). For a flight model, this weight could be reduced to 35.9 kg (79.3 lb) by the implementation of the following changes:

(1) Replace magnesium drum shells with beryllium.

(2) Remove Schjel-Clad residual adhesive on the backside of the blanket. The flight weight also takes into account that the dummy glass simulated cells are slightly heavier than actual solar cells.

The calculated values for the center of mass and the moments and products of the inertia are shown in Table 4.

## IV. System Electrical Performance Summary

The power-to-weight ratio of the array system is based on the generation of 2500 W of raw array power, while operating at 55°C under air-mass-zero 1.0-AU illumination and orientation within ±0.1745 rad of the sun. Cell efficiency is specified by the area performance criteria of 107.6 W/m$^2$ (10 W/ft$^2$) of gross module area. The solar cell is 0.02 cm thick and 2 × 2 cm square with bar contacts (3.8-cm$^2$ active area /cell). Figure 9 shows the typical solar array I-V curve based on the performance of these cells. This curve represents the expected beginning of life raw array power characteristics and includes a 6% reduction in short-circuit current to provide for array fabrication losses. The calculated maximum raw array power under these conditions is 2523 W at 102 V dc. To arrive at the maximum power available at the electrical interface on the center support, the following distribution losses must be accounted for:

(1) Array blanket bus strip series resistance losses.

(2) Slip-ring series resistance losses, including line losses within the storage drum and center support.

(3) Solar cell interconnect series resistance losses.

The effect of this combined series resistance is to reduce the maximum power by 51 W at a 55°C operating temperature. The effective series resistance of the slip rings and associated harnessing within the drum and

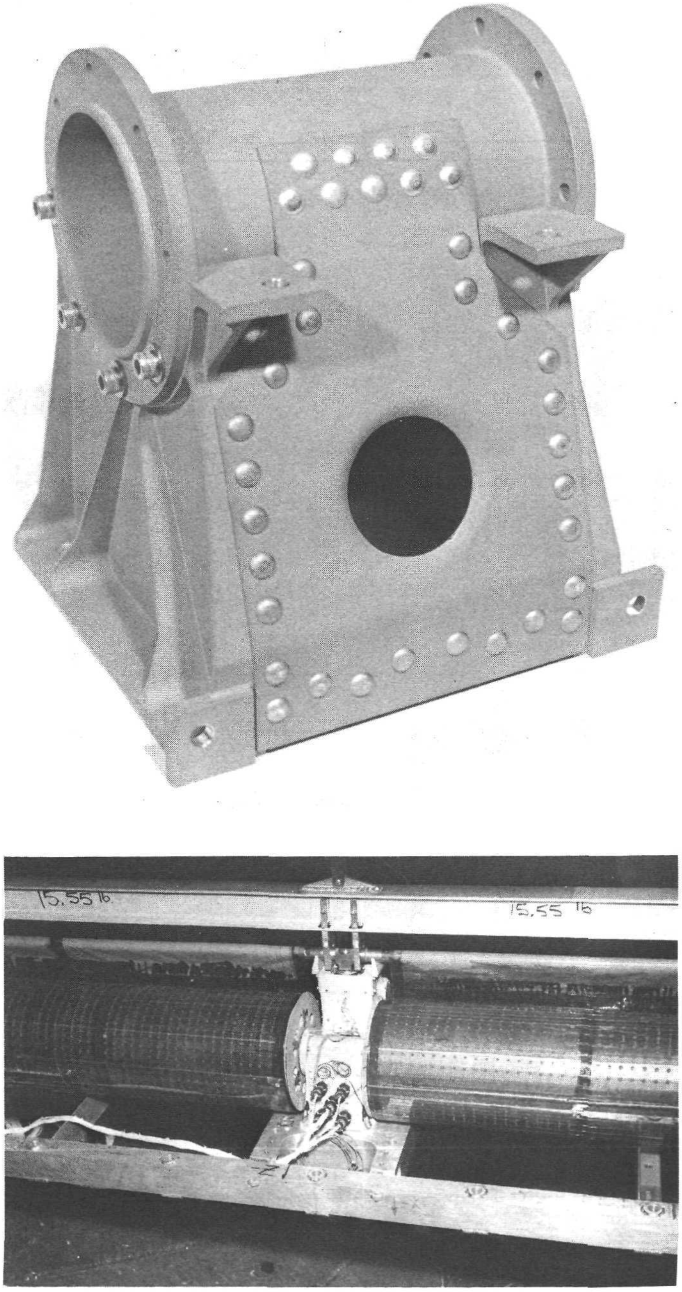

**Fig. 8. Center support: (a) component, (b) center support assembly**

Table 3. Actual mass summary (engineering model)

| Nomenclature | Mass, kg | Weight, lb |
|---|---|---|
| Center support | 0.66 | 1.46 |
| Leading edge member | 0.38 | 0.85 |
| Boom actuator | 2.41 | 5.32 |
| Boom extended element | 3.01 | 6.65 |
| Outboard end support (total for 2) | 1.86 | 4.1 |
| Drum assemblies including bearings, slip rings, and Negator springs (total for 2) | 7.98 | 17.6 |
| Left array blanket assembly | 10.53 | 23.22 |
| Right array blanket assembly | 10.59 | 23.36 |
| Total array mass | 37.42 | 82.56 |

Table 4. Summary of mass properties

| Properties[a] | Stowed | Deployed |
|---|---|---|
| Center of mass, cm | | |
| $X$ | −0.5 | +305.0 |
| $Y$ | 0 | 0 |
| $Z$ | +2.3 | + 7.9 |
| Moments of inertia about center of mass, kg-m$^2$ | | |
| $I_{XX}$ | 18.5 | 18.3 |
| $I_{YY}$ | 0.6 | 459.2 |
| $I_{ZZ}$ | 18.5 | 477.9 |
| Products of inertia about center of mass, kg-m$^2$ | | |
| $I_{XY}$ | 0 | 0 |
| $I_{XZ}$ | −0.01 | + 2.47 |
| $I_{YZ}$ | 0 | 0 |

[a]The coordinate system is shown in Fig. 1.

center support was measured during the system test program. Based on these measurements, a value of 0.02 Ω is used as the combined series resistance for both power ring circuits of a slip-ring assembly. Therefore, the total slip ring loss at maximum power is 6 W for the entire array. Accounting for these various array losses, the maximum net power available at the electrical interface on the center support is 2466 W.

## V. Out-of-Plane Deployed Dynamics

Because of the flexible nature of the deployed array and the possibility of adverse interaction with spacecraft attitude control systems, a significant effort was devoted to analyzing and measuring the deployed dynamics of the array. The actual test program was conducted in two parts. The first series of tests and analyses were conducted immediately following the completion of the array fabrication and concentrated on the out-of-plane modal characteristics of the deployed array. The results of this sequence of tests are described and compared with analytical predictions in this section.

Although in-plane mode measurements were conducted in the first modal test sequence, large discrepancies were found in both the modal test and analytical results for the in-plane mode. These discrepancies were caused by the highly nonlinear and very complex in-plane structural behavior of the array. To gain an understanding of this behavior, an additional combined analytical and experimental program was conducted. The results of this in-plane dynamic analysis effort are described in Section VI. The following discussion is limited to the analyses and tests made to determine the natural frequencies, mode shapes, linearity, and modal damping for out-of-plane motion of the array.

### A. Rationale

Because of the size and structural nature of the deployed array, it was considered impractical, if not impossible, to determine the zero-g natural frequencies and vibration modes in a 1-g test environment. A decision was therefore made to analytically model the array with a mathematical formulation which included the forces of gravity as a parameter that could be varied from zero to 1 *g* without significantly changing the character of the formulation. The mathematical model could then be correlated with measured 1-g modal test results, and, if found to agree, could be confidently used to extrapolate to the zero-g modal characteristics.

To minimize the effects of gravity and to remove aerodynamic effects, it was decided to run the deployed dynamics tests with the array deployed vertically downward within a large vacuum chamber. With this arrangement, the forces of gravity are superimposed on the normal zero-g blanket tension loads and merely result in a linearly varying tension distribution in the blanket and boom instead of the normal constant tension and compression distributions maintained by the Negator springs. The Negator springs were supplemented with additional springs to compensate for the weight of the blankets, permitting each drum to rotate in a normal manner. The normal 9-N (2-lb) per blanket tension load was maintained at the unconstrained leading edge member. Thus, the only effect of the gravity field is to vary the tension distribution in the blanket and boom. The boundary conditions associated with the blanket/LEM/boom attachment remain unchanged.

In addition to providing data for comparison with the analytical results, the deployed dynamics test was also designed to determine the linearity of the out-of-plane response with respect to excitation level and to provide data on system damping. It was decided to run tests in both ambient and vacuum environments in order to assess the effect of the aerodynamic loading on the natural frequency and damping.

## B. Mathematical Modeling

Because the mathematical model was the sole means of determining the zero-g modes of the array, and could only be correlated with measurements in the 1-g test configuration, it was important that the modeling technique be as accurate as practical, and be amenable to including the effects of gravity as a parameter. A finite element representation of the array was chosen for the analysis. Though various discretizations were used, the symmetric and antisymmetric models shown in Fig. 10 are typical. Each blanket is modeled by an array of rectangular finite elements, which describe the out-of-plane stiffness caused by the imposed blanket tension. The boom and LEM are similarly modeled by standard beam-column elements, which describe both the bending stiffness and the geometric stiffness caused by the axial preload. For a detailed description of the finite element models and typical results, see Ref. 2 (Section 4.3). A comparison of the zero-g and 1-g modes is given in Ref. 3 (Section 2.13).

More recently, the symmetric and antisymmetric models have been combined in order to allow unequal blanket tensions for the two blankets, and rectangular plate elements have been added to account for the bending stiffness of the blankets. These modifications, discussed in depth in Ref. 4 (Section 4.3.4), have been found necessary because the unequal tensions in the actual array prevent the formation of purely symmetric and antisymmetric modes.

## C. Test Approach

To meet the above objectives of providing damping and linearity data and modal data for comparison with the analytical results, modal tests were conducted with the array deployed vertically downward in the 9.8 × 16.5 m (32 × 54 ft) Space Simulator at the General Electric, Valley Forge Space Center. Since array length was also parameterized in the mathematical model, a deployed test length of 8 m (26 ft) was used in order to limit most of the test hardware to the workspace below the parting line of the vacuum chamber lid. The conceptual arrangement of the test is shown in Fig. 11. The array was suspended from a support fixture, which included a bearing system that could be arranged to provide both in-plane and out-of-plane horizontal motion and rotation about the vertical boom axis. A dc-coupled exciter suitable for vacuum operation was used for the test. Auxiliary equipment to provide stable sinusoidal motion down to 0.008 Hz and 0.006-cm (0.0025-in.) motion (double amplitude) was used, with a sweep rate capability down to $10^6$ s/decade.

Array displacements were measured with eight Optron Model 800 optical trackers modified to allow operation in vacuum. The trackers had no physical contact with the test specimen, and had the capability of measuring displacements in two directions over the frequency range from dc to 10 kHz. The units used for these tests had the capability of resolving motions as small as 0.0025 cm (0.001 in.). Two trackers were focused on the ends of the leading edge member and were fixed. Six were mounted on a scanning bar which traversed the length of the system, and could be positioned at 10 equally spaced span locations. White paper targets were mounted on the cell side of the solar array blankets to provide the contrast needed for the operation of the trackers.

In addition to more conventional test equipment, a single-channel low-frequency wave analyzer was used to provide real-time in-phase and quadrature analyses during the frequency sweeps. (For a more complete description of the test setup, see Ref. 4, Section 4.3.2.)

## D. Summary of Results

In the test sequence, the vacuum tests in each axis were preceded by tests in air to allow visual observation of the modes and measurement of the effect of the aerodynamic coupling. The ambient tests provided valuable visual verification of and insight into the complex higher-order modes. However, vacuum testing was found to be a definite requirement for accurate measurement of mode shapes, frequencies, damping, and nonlinearities. The effective damping and mass loading due to aerodynamic coupling led to measured frequencies generally 25% lower than the corresponding vacuum values.

Figures 12 and 13 summarize the results of the symmetric and antisymmetric sweep test in vacuum, and represent an overlay of the quadrature response of the left

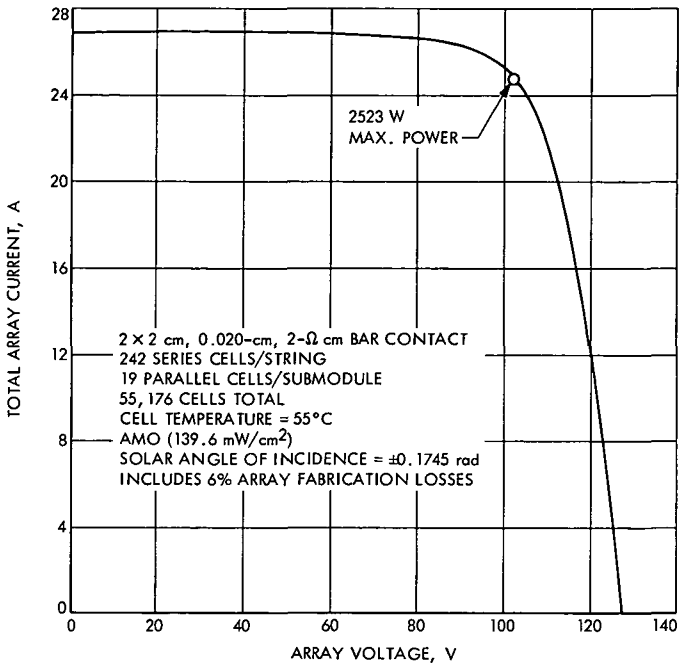

**Fig. 9. Typical subsolar array I-V curve**

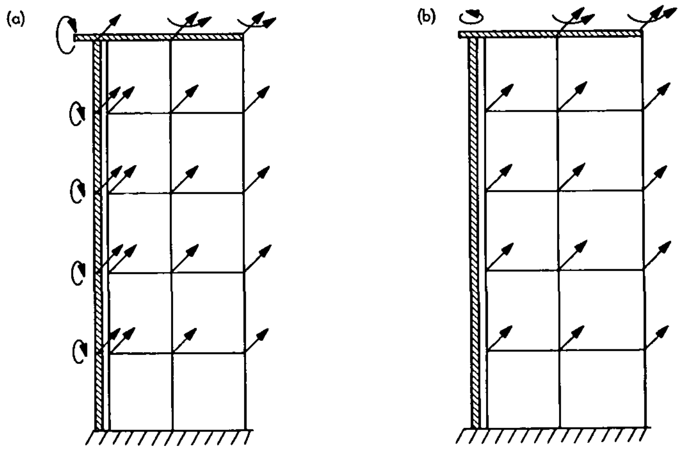

**Fig. 10. Typical finite element models: (a) symmetric, (b) antisymmetric**

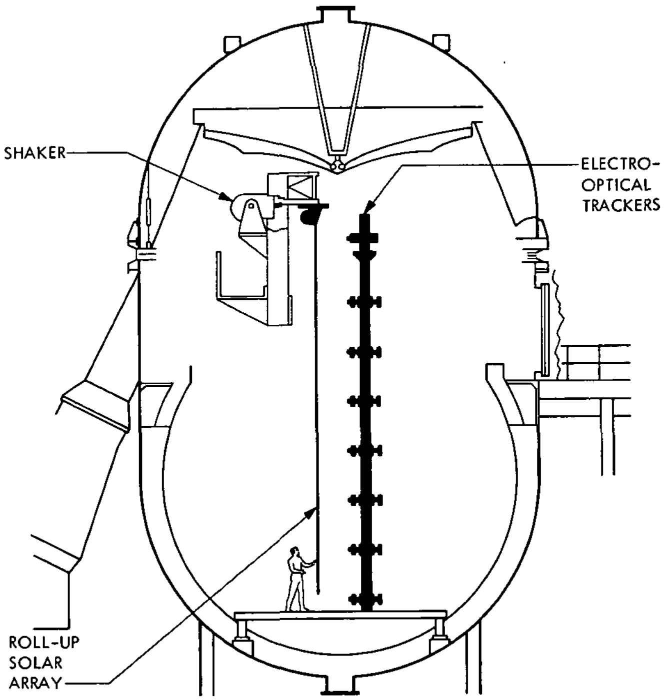

**Fig. 11. Deployed dynamics test setup**

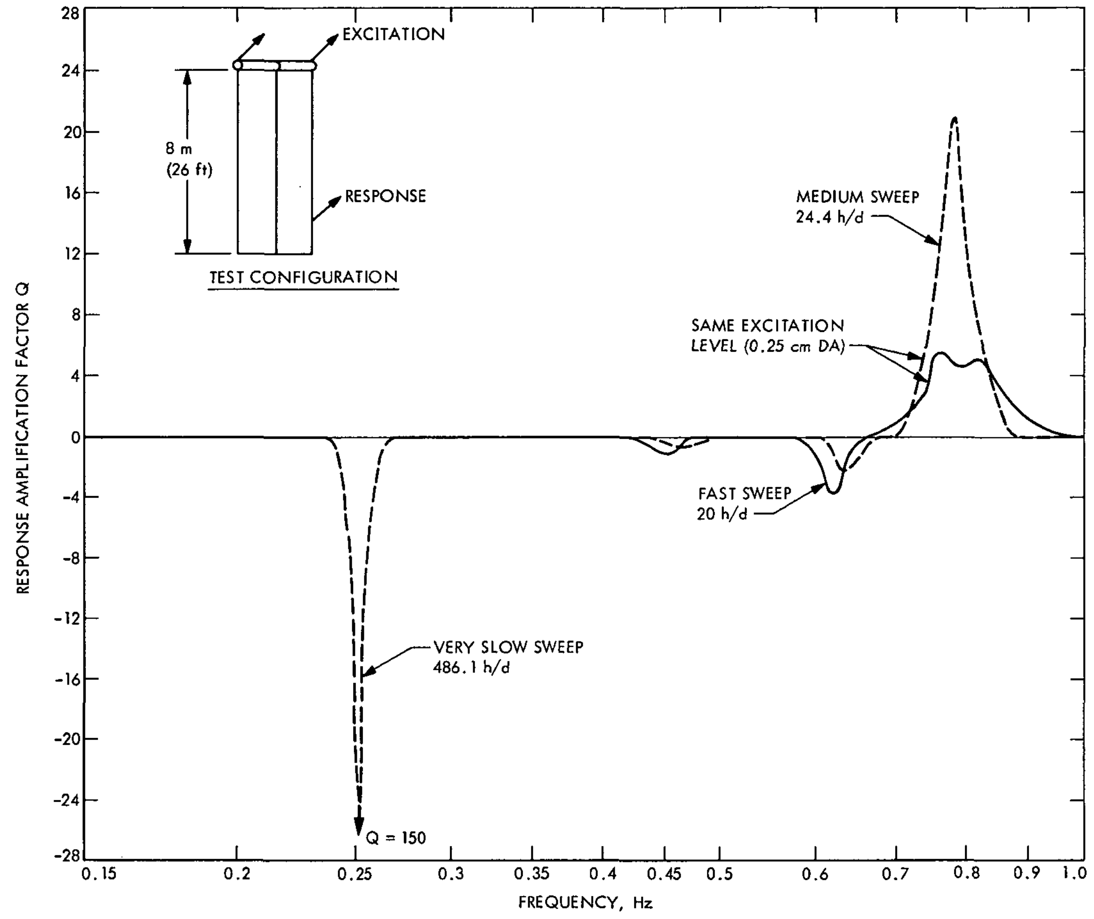

**Fig. 12. Quadrature response to out-of-plane symmetric excitation**

edge of the left blanket at the 80% span position. The first symmetric bending frequency, indicated by the response peak at 0.251 Hz in Fig. 12, agrees within 1% with the analytically predicted frequency. This is considered excellent agreement. However, the first antisymmetric (torsion) frequency occurred at 0.174 Hz, (Fig. 13), 30% lower than the predicted value of 0.232 Hz. The first symmetric and first antisymmetric modes are pictured in Fig. 14. The correlation between the frequencies and mode shapes for higher-order modes was poorer than first expected. A significant difference in the higher-order modes was the absence of symmetric/antisymmetric pairs.

Measured damping ratios ranged from about 0.5% for the first symmetric and torsion modes up to 1 to 2% for the higher-order modes.

It can be seen from Figs. 12 and 13 that the frequencies and response amplitudes were quite sensitive to input amplitudes and sweep rates. This nonlinearity significantly complicated attempts to dwell at resonances for mode shape measurements. In addition, the low damping and low-frequency range required very long sweep times, ranging from 1.3 to as high as 100 h/decade. The response nonlinearity and long sweep times, combined with the pump down and vent times for the vacuum chamber operation, made the modal analysis very time-consuming and prevented more in-depth studies of the higher-order modes. Measurement of the complex higher-order modes was also handicapped because the instrumentation was arranged anticipating symmetric/antisymmetric modes.

## E. Conclusions

In the analytical studies which preceded the test program, the deployed array was modeled by symmetric and antisymmetric models in order to reduce the size of the computational problem. The models also assumed the tension to be evenly distributed across each blan-

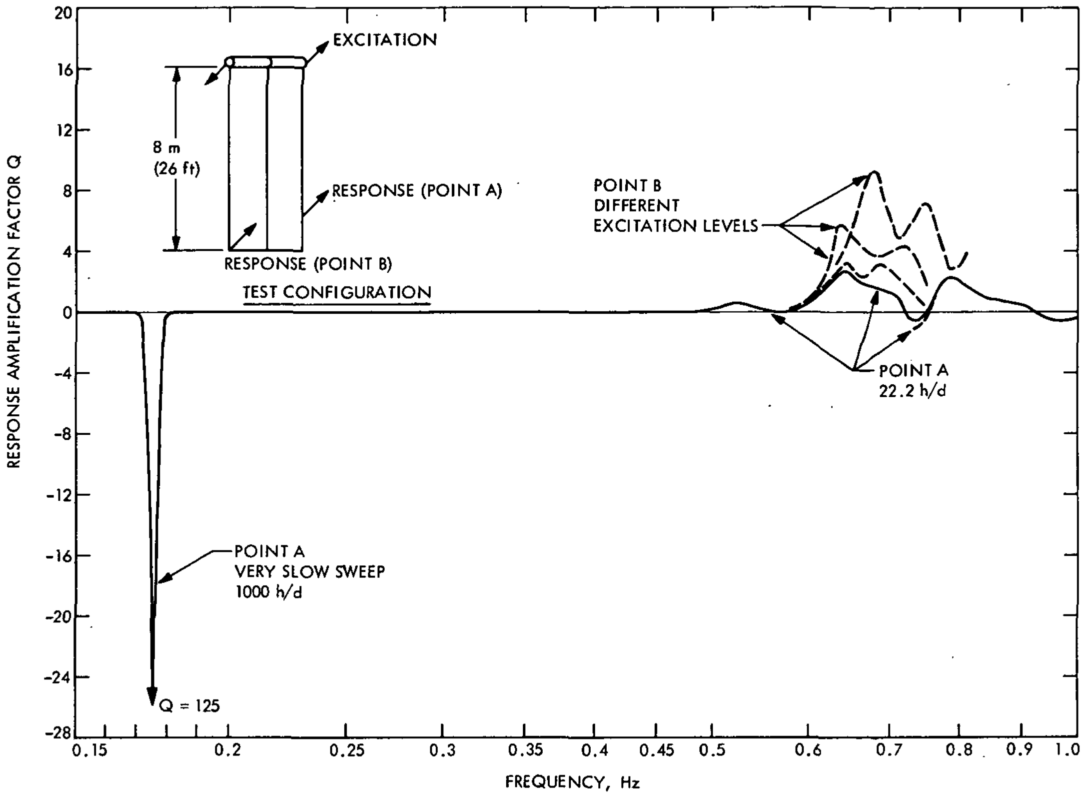

**Fig. 13. Quadrature response to out-of-plane antisymmetric excitation**

ket's width and, with the symmetry assumption, to be equal in the two blankets. In addition, the bending stiffness of the blanket material was assumed to be negligible compared to the stiffness due to the imposed tension.

Although these assumptions are reasonable for an ideal array, they were not satisfied by the array in its test configuration, and are expected to have contributed significantly to the difference between the analytical and experimentally measured modes. The symmetry and uniformity assumptions were made particularly inappropriate by the following factors:

(1) Different weights for the two blankets and uncertain amounts of friction in the blanket tensioning mechanisms were expected to lead to unequal tensions in the two blankets.

(2) Downward bending, or drooping, of the blanket storage drums under the weight of the blankets is considered to have resulted in a nonuniform tension distribution at the attachment between the blankets and the drums.

(3) Misalignment between the leading edge member and the blankets is known to have resulted in a nonuniform tension distribution along the blankets' attachment to the LEM.

(4) Because of the inelastic nature of the blankets relative to in-plane displacements, the nonuniform boundary tensions are assumed to have resulted in significant tension nonuniformities throughout the blankets.

In order to explore the significance of the nonuniform tension distributions and the effect of the blankets' bending stiffness, a more detailed analysis of the array was conducted using an expanded dynamic model. The direction of the study was focused at the following four general areas:

(1) The effect of the bending stiffness of the blanket material.

(2) The effect of the magnitude and symmetry of the blanket tension at the LEM attachment.

(3) The effect of nonuniform tensions within the blankets.

   (a) Top outside corners slack.

   (b) Bottom outside corners slack.

TORSION (ANTISYMMETRIC)

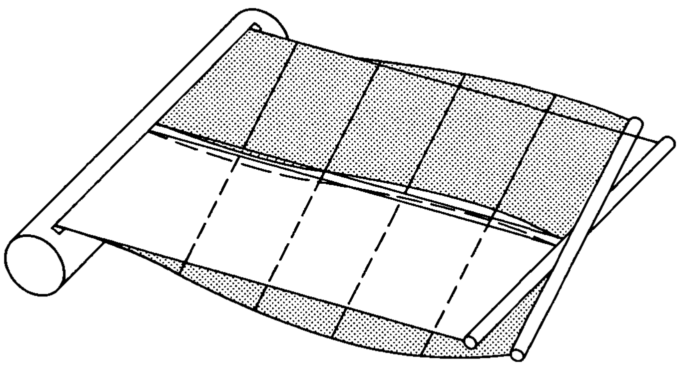

BENDING (SYMMETRIC)

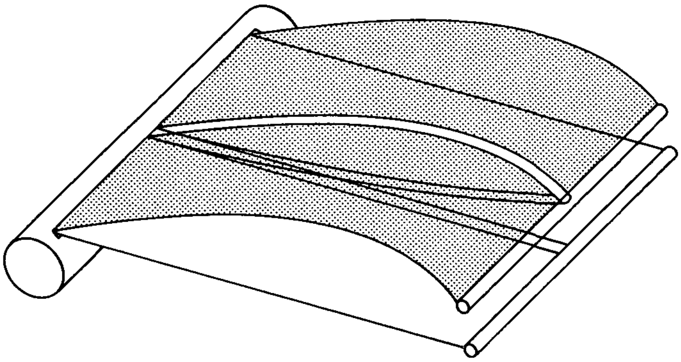

**Fig. 14. First symmetric and antisymmetric out-of-plane vibration modes**

    (c) Top outside corners and sides slack.
    (d) Top and bottom corners and sides slack.
(4) The effect of increased blanket bending rigidity due to edge curl.

The results of each of these areas of study are summarized in detail in Ref. 4 (Section 4.3.4). At least two general conclusions can be drawn, one about the sensitivity of the modes to the blankets' bending stiffness and tension distributions and the other concerning our current modal prediction capability.

The first conclusion is that the array's lowest symmetric and antisymmetric resonant frequencies are rather insensitive to large variations in the blankets' bending rigidity and tension uniformity, whereas the higher-order modes are very sensitive to both the bending rigidity and the tension uniformity. This indicates that, although the primary resonances should be quite predictable, the higher-order resonances will be generally dependent on a number of unknown and uncertain parameters such as the blankets' tension distribution, the Negator spring torque, and the blankets' bending rigidity. Since all of these parameters may vary with both time and temperature, it is doubtful whether the higher-order modes can be predicted with confidence, even with an exact mathematical model because of the difficulty of accurately predicting the state of the structure.

Adding to the problem, of course, is the possible inaccuracy of the mathematical representation of the structural properties of the array. Although the finite element model used in the study appears to predict the primary resonances accurately, certain inconsistencies arise when the higher-order modes are compared with the experimentally measured ones. The primary difference is the edge flapping which appears in the analytical modes when the outer edges of the blankets are loosened as required to match the first torsion frequency. Intuitively, the edge flapping behavior is expected, and it is the experimentally observed behavior which seems inconsistent.

As a means of checking the accuracy of the finite element analysis, the blanket substructure model was also used to predict the first mode resonance of a single blanket hanging vertically with the lower end free. This vibration mode was also measured experimentally during the modal test program. Since the mode represents blanket pendulum motion with no tension at the LEM attachment, its frequency should provide a lower bound for the first torsion mode, which exhibits the same pendulum motion but has an additional tension applied to the lower edge.

As expected, the free blanket frequency predicted by the analysis agreed with the array's first torsion frequency calculated using zero LEM tension and zero LEM mass. In addition, it agreed within 2% with the free blanket frequency determined experimentally during the modal testing. Since the experimentally measured torsion frequency was nearly 20% lower than the free blanket frequency, there is considerable justification for assuming the presence of a nonuniform tension distribution. Small errors in representing the array's mass properties, for example, could not lead to the 30% lower frequency obtained experimentally for the first torsion mode.

Considering the above, one must thus conclude that although certain inconsistencies exist, the current finite element model appears to provide adequate prediction capability for the array's primary resonances. However, the capability and desirability of predicting the higher-order modes is uncertain at this time. A chief difficulty is the sensitivity of the higher-order modes to small changes in the blanket tension distributions.

## VI. In-Plane Deployed Dynamics Tests

In a preliminary study, an attempt was made to model the in-plane dynamics of the deployed array using rectangular membrane finite elements with in-plane displacement coordinates (Ref. 3, Section 2.1.3, and Ref. 5, Section 2.1.3). However, comparison with the in-plane vibration mode measured during the deployed modal test program indicated serious deficiencies in the model. The primary difficulty was that the linear analysis used to model the array could not account for the shifting blanket tension which dominated the in-plane stiffness in the 1-*g* field test configuration. In addition, the linear finite element model had to treat tension and compression in the array blankets similarly, whereas the actual blankets are quite stiff in tension but are incapable of being loaded in compression. Because of these difficulties and the importance of accurately defining the array's in-plane vibration characteristics, a supplemental program was conducted in order to further explore the in-plane dynamics of the array. Detailed results are presented in Ref. 6.

### A. In-Plane Stiffness Analysis

Because the mass of the array was considered to be well described by the preliminary analysis, primary emphasis was placed on understanding the in-plane stiffness of the deployed array. Initial work with a desktop model indicated that the stiffness was due in part to a shifting of the blanket tension during in-plane displacement. Following this observation, the 1.2-m (4-ft) wide Phase I roll-up solar array demonstration model was used in a series of experiments designed to explore the in-plane stiffness phenomenon. This unit is half the width of the 23-$m^2$ (250-$ft^2$) array (RA250) and has bare Kapton substrates to simulate the cell blankets. Because of their light weight, the bare Kapton sheets maintain tension distributions similar to those in the actual cell blankets in zero gravity. The boom and drums are essentially identical to those in the RA250 array, except that the drums are only 0.6 m (2 ft) wide.

An understanding of the in-plane structural characteristics was achieved as a result of the experimental program. Measurements were made of both the complete solar array and of the bi-stem boom as a separate element. The bi-stem was found to exhibit considerable hysteresis and nonlinear stiffness due to friction-controlled root flexibility. For small deflections, static friction appears to inhibit both root flexibility and relative motion of the two elements, and the bi-stem behaves like a true cantilever beam. For larger deflections, friction at the root is overcome and the lower root stiffness reduces the stiffness of the cantilevered bi-stem. The effects of root flexibility were apparent in measurements of the boom stiffness and in measurements of the rotation at the boom tip.

Consider the formula

$$\theta = a\delta/L \tag{1}$$

where

$\theta$ = angular displacement of bi-stem tip

$a$ = parameter

$\delta$ = linear displacement of bi-stem tip

$L$ = length of bi-stem

The parameter $a$ equals 1 for a rigid rod hinged at one end and 1.5 for a simple cantilever beam with a transverse load at the tip. For the bi-stem, values of $a$ equal to 1.28, 1.32, and 1.37 were measured for lengths of 2.44, 3.35, and 4.88 m (8, 11, and 16 ft). A root stiffness $K_R$ of 1500 Nm/rad (1100 lb ft/rad) and a section stiffness $EI$ of 910 $Nm^2$ (2200 lb $ft^2$) were determined from the experimental data. The section stiffness is about 14% lower than the value reported by the vendor for the 3.4-m (1.34-in.) bi-stem element.

In tests of the in-plane stiffness of the entire array, boom stiffness was found to be a major contributor, but stiffness resulting from blanket tension redistribution dominates for small displacements. When the array deflects in-plane, as shown in Fig. 15, the high longitudinal rigidity of the boom, the rolling ability of the drums, and the inability of the blankets to withstand compression cause the blankets to move vertically at the drum end and horizontally at the boom tip. Because the blankets are extremely rigid in tension, the shaded areas in Fig. 15, which remain in tension during moderate displacements, must move as rigid bodies. Analysis of the movement pattern indicates that the motion is a pure rigid body rotation about the root of the boom. Since the leading edge member is attached to the blankets, and the boom to it, the tip of the boom is constrained to move so that the tip deflection angle $\theta$ is related to the tip deflection $\delta$ by $\theta = \delta/L$ ($a = 1$ in Eq. 1).

For large in-plane displacements, there are three regions of the system force/deflection behavior. In the small deflection region, designated Region 1, the load deflection characteristic is reasonably linear and the stiffness is the highest observed. This region is a transition region, where the initially uniform blanket tension distributions at the drums shift toward the drum ends, as indicated in Fig. 15. Since the drums apply a constant force to each blanket, this tension shift applies an increasing restoring torque to the array which adds to that due to bending of the bi-stem boom. The mechanism that governs the rate at which the tension shifts with increasing array deflection is still not understood. However the empirical studies established for the array tested that the portion of the Region 1 stiffness attributed to the shifting tension distribution is proportional to the square root of the blanket tension and inversely proportional to the square of the array length. Since the mechanism is unknown, it is not known whether this relationship holds for arrays other than the test model.

Region 2 of the in-plane force/deflection relationship starts when the tension has shifted entirely to the ends of the drums. For larger array deflections, the application point of the resultant tension load is known to remain fixed at a point midway between the drum ends, as shown in Fig. 16. At the outer end of the array, the blankets constrain the leading edge member and boom tip to rotate as a rigid body pinned at the root of the boom. In order to impose this constraint, the blanket tension must apply a restoring moment to the boom tip by shifting along the leading edge member by an amount $\Delta$, which increases linearly with increasing in-plane array deflection (Fig. 16). The tip moment required by the constraint $\theta = \delta / L$ was determined for an axially loaded boom with root stiffness $K_R$, and an expression was obtained for the tension shift $\Delta$ at the leading edge member as a function of the array deflection $\delta$. Combining these data with the known shear force in the boom, just below the tip, gives the following expression for the array in-plane force/deflection relationship in Region 2:

$$F_2 = \left[ \frac{4EI}{L^3(1 + 4\alpha)} - \frac{4T}{15(1 + 4\alpha)^2 L} \right] \delta + \frac{TW}{L} \qquad (2)$$

where

$F_2$ = transverse force, N

$\alpha = EI/K_R L$

$W$ = blanket width, m

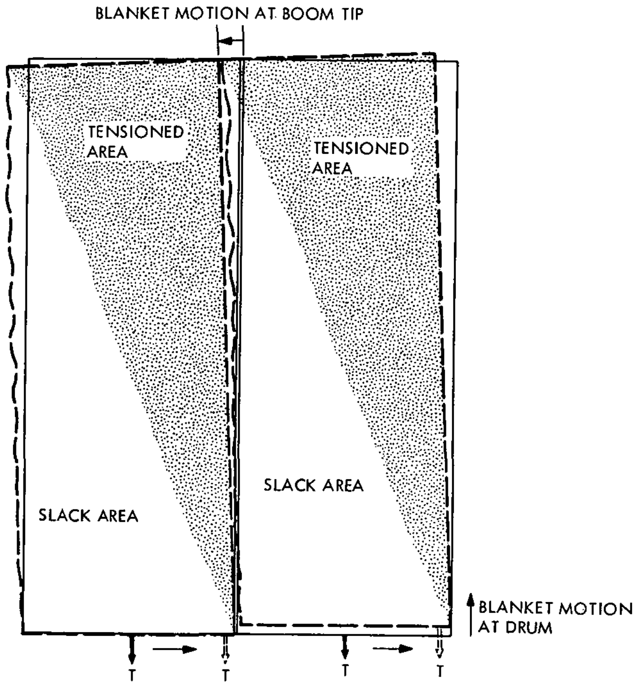

Fig. 15. In-plane deflection mode

$EI$ = section modulus of bi-stem, $\mathrm{Nm}^2$

$K_R$ = root stiffness of bi-stem, Nm/rad

$L$ = deployed length, m

$T$ = blanket tension, N

$\delta$ = tip deflection, m

Region 3 of the force deflection relationship occurs when the blanket tensions at the leading edge member reach the edges of the blankets ($\Delta = W/2$) and the tension forces can no longer constrain the boom tip rotation. This occurs when the array deflection $\delta$ exceeds the value defined by

$$\delta \text{ (for region 3)} \geq W / \left[ \frac{2EI}{TL^2(1 + 4\alpha)} + \frac{(1 + 12\alpha)}{15(1 + 4\alpha)^2} \right] \qquad (3)$$

At this point, the system stiffness approaches the stiffness exhibited by the axially loaded bi-stem without tip constraint. This stiffness is roughly 75% of that in Region 2. For the 23-$\mathrm{m}^2$ (250-$\mathrm{ft}^2$) prototype array, the Region 3 stiffness is of little consequence because it is achieved only with in-plane tip displacements greater than about 0.6 m (2 ft).

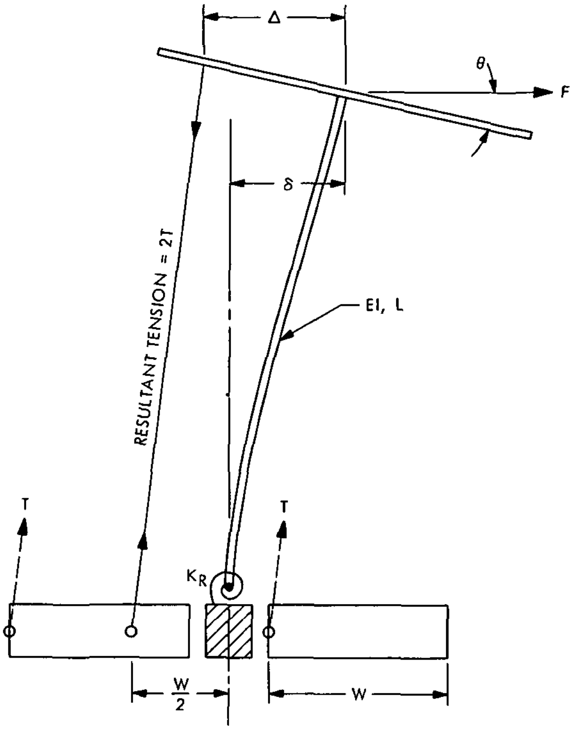

Fig. 16. Region 2 in-plane force diagram

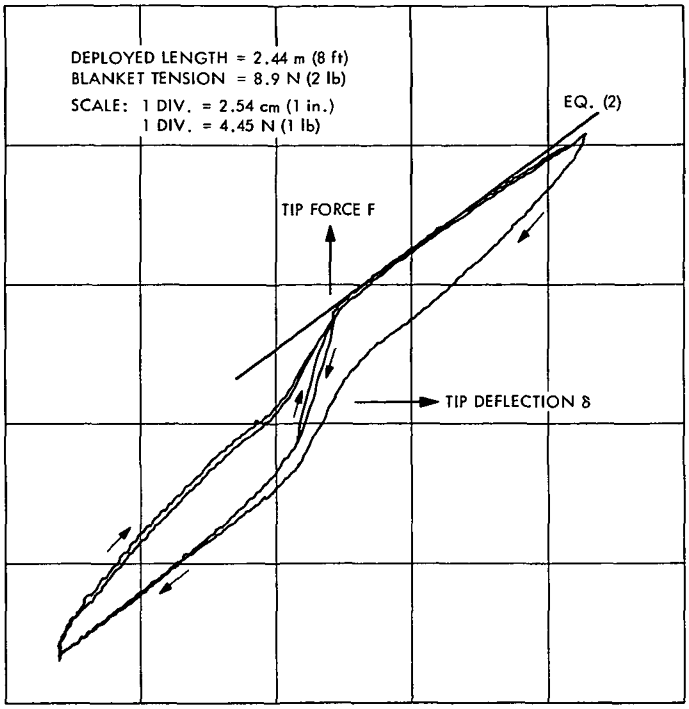

Fig. 17. Measured in-plane force-deflection relationship

Figure 17 displays a pair of typical force/deflection plots obtained experimentally for the Phase I demonstration model array. The small inner loop is a force/deflection cycle entirely within Region 1, where, in addition, the deflection does not reach a value large enough to break the root of the boom free from static friction. The bi-stem acts as a tip-constrained cantilever with near infinite root stiffness in this cycle. The larger force/deflection cycle contains all three regions and exhibits the hysteresis which is typical of the in-plane motion when the static friction at the boom root is overcome. The increased stiffness (curve slope) when the motion is reversed at the extremes of the cycle is caused by the temporary loss of the root flexibility to static friction. The effect of the friction-controlled flexibility at the boom root is also the cause of the difference between the Region 1 stiffness in the small and large deflection cycles. The Region 2 stiffness defined by Eq. (2) is indicated in the figure. Note that it agrees very well with the measured Region 2 stiffness and is about one quarter of the small-deflection Region 1 stiffness which does not include root flexibility.

## B. In-Plane Dynamic Analysis

In the stiffness analysis, it was noted that the in-plane motion is essentially a rigid body rotation about the root of the boom. As a result, the inertia associated with the in-plane motion is quite accurately described in terms of the rigid body inertias of the individual components. For a typical array, the inertia about the root of the boom is sufficiently described by

$$I = M_{\mathrm{BLK}} \frac{W^2 + 4L^2}{12} + \frac{M_{\mathrm{BM}} L^2}{3} + M_{\mathrm{LEM}} L^2 \tag{4}$$

where

$I$ = inertia of array about boom root, kg/m$^2$

$M_{\mathrm{BLK}}$ = total mass of both blankets, kg

$M_{\mathrm{BM}}$ = mass of deployed boom, kg

$M_{\mathrm{LEM}}$ = mass of leading edge member, kg

$W$ = total width of array, m

$L$ = deployed length of array, m

To make it compatible with the above inertia, the in-plane stiffness is best lumped as a torsion spring at the root of the array. Because the Region 1 stiffness is not known, preliminary analyses to date have used the Region 2 stiffness from Eq. (2) to provide a lower bound on the natural frequency of the in-plane vibration mode.

When converted to a torsion stiffness, the Region 2 stiffness reduces to

$$K_2 = \frac{4EI}{L(1 + 4\alpha)} - \frac{4TL}{15(1 + 4\alpha)^2} \qquad (5)$$

where

$K_2$ = in-plane stiffness in Region 2, Nm/rad

$EI$ = boom cross-sectional stiffness, Nm$^2$

$T$ = blanket tension per side, N

$L$ = array length, m

$\alpha = EI/K_r L$

$K_r$ = boom root stiffness, Nm/rad

Natural frequencies calculated using Eqs. (4) and (5) were found to agree very well (within 5%) with large displacement frequencies obtained by displaying the test model and suddenly releasing it. As the amplitude damps down, the Region 1 stiffness dominates and the frequency increases. The maximum frequency achieved for very small displacements is about double the frequency defined by the Region 2 stiffness.

The effective damping of the in-plane mode was found to be very high, with an equivalent viscous damping coefficient of approximately 10%.

### C. Conclusions

The in-plane force/deflection characteristic of the roll-up solar array is a complicated nonlinear function involving boom bending, blanket tension redistribution, root flexibility, and friction effects. The in-plane stiffness of the cell blankets is much higher than the stiffness of the other components and can be accurately assumed to be infinite. However, the high in-plane rigidity of the blankets does not significantly stiffen the array as a whole because the blankets are attached to very soft tensioning mechanisms (Negator springs). The in-plane stiffness of the array is controlled primarily by boom bending and blanket tension redistribution. In general, the lowest in-plane vibration mode has a natural frequency only slightly higher than the lowest out-of-plane mode. However, it has much higher damping.

## VII. Environmental Tests

The engineering model was subjected to an environmental test program that included the following tests:

(1) Pyrotechnic-induced shock.

(2) Thermal vacuum series.

(3) Acoustic noise.

(4) Stowed vibration.

These tests were performed in the order listed, with intervening electrical and mechanical inspections. Detailed results are included in Ref. 4.

### A. Pyrotechnic-Induced Shock Tests

The pyrotechnic-induced shock test was conducted by simultaneously firing both separation nuts (each armed with two active squibs) on the outboard end supports. The response of the system was determined through the use of shock spectrum analysis to determine the necessity for further shock-type testing to synthesize the specified shock pulse shown in Fig. 18.

The highest accelerations were measured on the movable arms, 10.16 cm (4 in.) from a separation nut assembly. Acceleration levels of 6000 and 2500 *g* (O-P) were recorded, which is approximately equal to shock levels measured on the array handling frame interface with the outboard end supports. The shock level rapidly decreased in magnitude with distance from the shock source. Shock levels on the drums at 100% span (near pyrotechnics) were 1365 *g* (O-P); at 0% span near the outer support, they dropped to 124 *g* (O-P). The blanket outerwrap (about 10 cm from the outboard end), the center support structure, and the drum bearing support shaft all experienced acceleration levels of 125 *g* (O-P) or less. This attenuation resulted from the lack of high-frequency transmissibility across the soft blanket, and the distance between the shock source and the response points monitored on the center support.

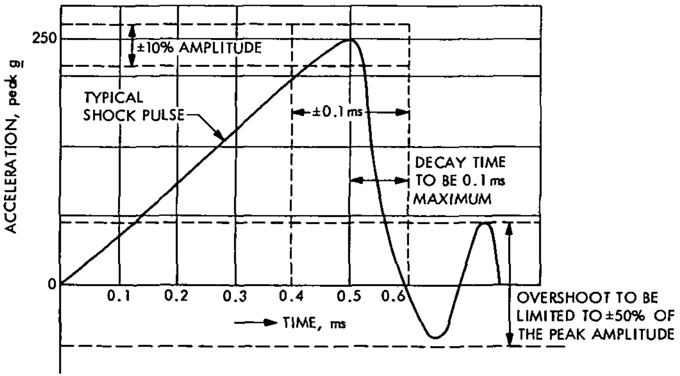

NOTE: SOME LATITUDE IS ALLOWABLE FOR THE WAVE SHAPE OF THE SHOCK PULSE. HOWEVER, IT IS DESIRABLE THAT THE SHAPE CONFORM TO THAT OF A TERMINAL PEAK SAWTOOTH AS NEARLY AS PRACTICAL.

**Fig. 18. Shock pulse**

Firing the separation nuts induced acceleration loads comparable to those induced in spacecraft structures by the firing of other pyrotechnical release devices. At the outboard end supports, the shock spectrum of the array pyrotechnics is higher than that resulting from the 250-g, 0.5-ms terminal sawtooth pulse defined in Fig. 18. In the center support region, the shock spectrum from the separation nut actuation is approximately equivalent to the spectrum of the sawtooth pulse above 2000 Hz and approximately 50% of the spectrum of the sawtooth below 2000 Hz.

## B. Thermal Vacuum Test Series

The engineering model was subjected to a series of thermal vacuum tests consisting of the following segments:

(1) Deployed transients.

(2) Low-temperature stowed.

(3) Low-temperature deploy and retract.

(4) Stowed transient and high-temperature soak.

(5) High-temperature deploy and retract.

The deployed array transient test was performed without incident. An example of the temperature versus time histories for two active solar cell modules is shown in Fig. 19. All active solar cell modules had similar transient response temperature histories. In all cases, the warmup to 140°C was performed by first turning on the lamps at a very low voltage to allow the filaments to heat up before applying full voltage. This procedure was necessary to avoid blowing fuses as a result of the high inrush current associated with the cold lamp filaments. This turn-on procedure caused the step-like appearance of the temperature rise plots for active solar cell modules.

During the low-temperature stowed test, it became apparent that the specified low-temperature extreme of −130°C on the control thermocouple could not be reached within a reasonable period of time. Therefore, this phase of the test was discontinued when the control thermocouple reached −113°C.

The low-temperature deployment of the array was initiated when the temperature recorded on the outboard end support adjacent to the $-Y$ separation nut was −60°C.

Deployment of the array was accomplished without incident. The motor temperature was −53°C immediately prior to deployment, with a 21°C rise recorded during the deployment. The bi-stem was then retracted from the fully extended position, but the retraction was stopped 195.6 cm (77 in.) short of the fully stowed position because of an apparent billowing of the $+Y$ blanket, as viewed via the closed-circuit TV camera. At the end of this retraction, the motor temperature was −21.6°C. When the chamber was entered to examine the test specimen, the major portion of the $-Y$ blanket was found draped on the chamber cryopanels. The $+Y$ blanket was in a slightly billowed condition, but the movement of personnel in the chamber was enough to cause the $+Y$ drum to rotate and rewrap this blanket in its normal stowed configuration. More detailed examination of the $-Y$ blanket revealed that a pull-apart thermocouple connector was lodged in the wrapped blanket in such a way as to prevent the drum from rotating. The failure to secure this connector to the bi-stem housing had evidently caused the $-Y$ blanket rewrapping problem. However, the test condition should not have caused the slight billowing of the other blanket.

Some typical results of the stowed transient test are shown in Fig. 20. Subsequent post-test inspection of both array blankets revealed that localized heating of the blanket had occurred as a result of the high-temperature stowed test. Areas of scorched adhesive were indicative of temperatures in excess of 176.6°C. Two active solar cell modules were situated within an overheated area at the same longitudinal station on the blankets. One of these modules suffered extensive lifting of the interconnect top contact due to solder melting in the overheated area. This condition would not have occurred if the array blankets had been completely covered with solar cell modules instead of optically transparent dummy glass platelets. The anomaly is attributed to a "greenhouse" phenomenon which resulted when visible and near-infrared energy from the heating lamp array was transmitted through the dummy glass and was trapped inside, causing localized high temperatures on the inside wraps of the stowed array blankets. The cause of the overheating is discussed in Refs. 4 and 6. The high-temperature deployment and retraction of the array were performed satisfactorily.

## C. Acoustic Noise Test

The stowed array was to be exposed to 60 s of random incidence reverberant sound, with an overall sound pressure level of 150 dB. During the test runs, the acoustic environment at various locations in and around the array and the response of the system were monitored.

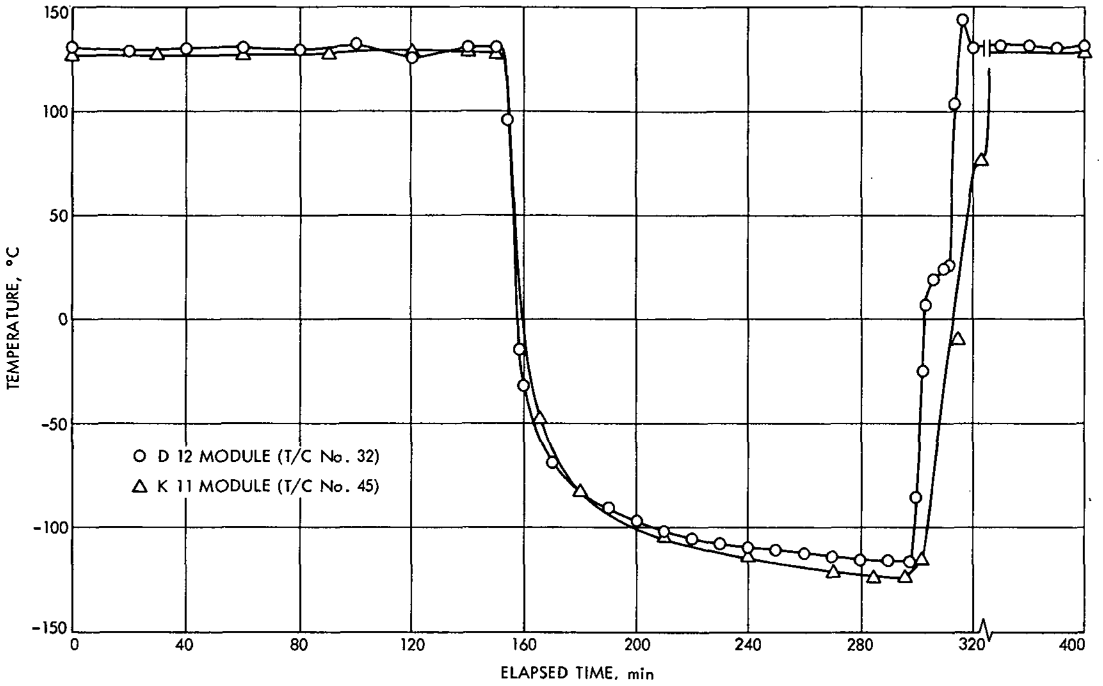

Fig. 19. Deployed transient temperature history

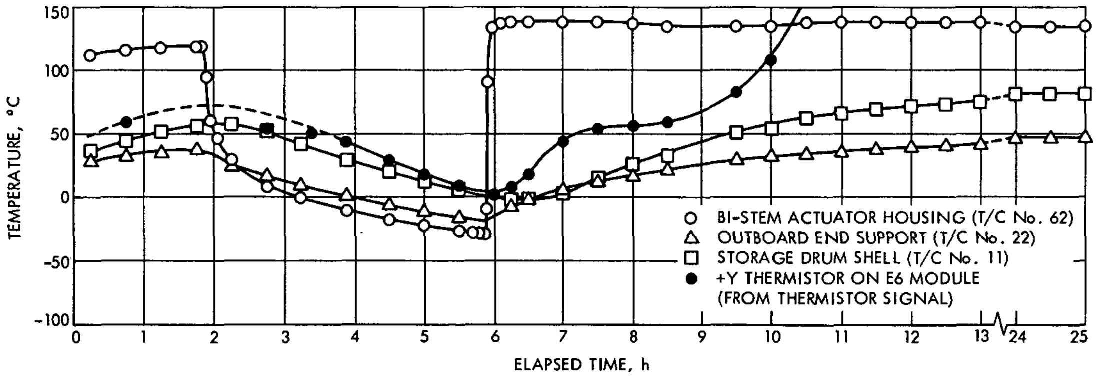

Fig. 20. Stowed transient temperature history

The test specimen, fully instrumented and secured to its holding fixture, was suspended from a spreader bar using shock cord, so that the natural frequency of the suspension system was less than 5 Hz. A first test run at 130 dB overall was made to check the spectrum shape with the actual test specimen in place. The second and third test runs of 30 s each were at full level. The test environment during these runs is shown in Fig. 21. Since the test level could not be increased without extensive effort, a 30-s penalty run resulted in a 147-dB overall SPL; so a second 30-s penalty run was performed. The overall level of each transducer is summarized in Table 5.

The response of the system indicates that an acoustic test of this type should be retained as a system test environment for future lightweight solar array assemblies to provide high-frequency excitation of the solar cell blankets.

## D. Stowed Vibration Test

During this test series, the array was subjected to qualification levels of sinusoidal and random vibration spectra as defined in Fig. 22. In addition, low-level sinusoidal sweeps were performed to locate stowed array resonant modes below 100 Hz.

The stowed vibration test was performed first in the *Y*-axis (parallel with the storage drum axis), then in the *Z*-axis (normal to the plane of the deployed array surface), and finally, in the *X*-axis (parallel to the axis of the deployed bi-stem boom). For each of these orientations, the testing was substantially identical and consisted of the following:

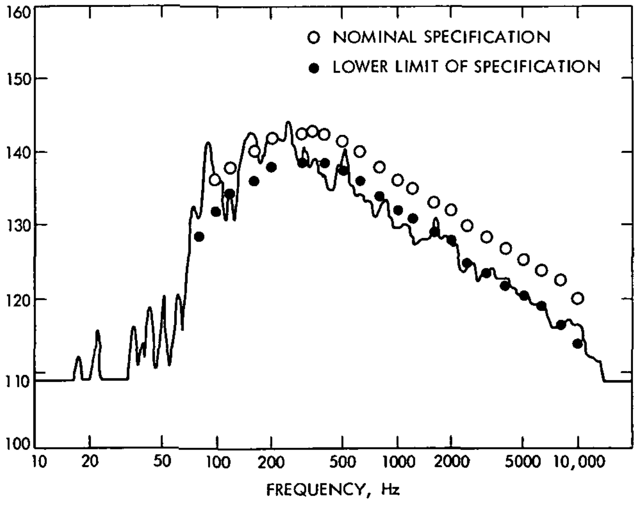

**Fig. 21. Spectrogram of input acoustic field during Run 3**

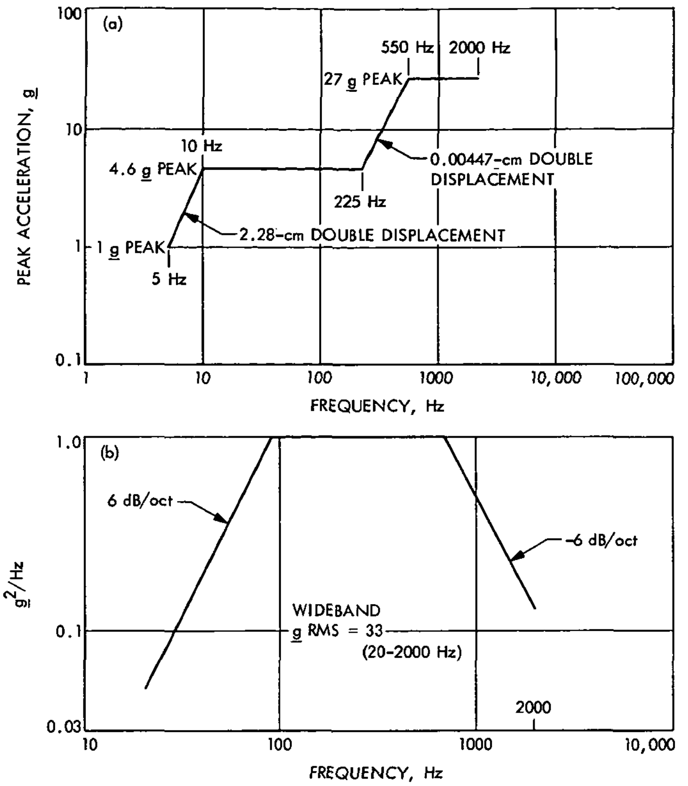

**Fig. 22. Specified qualification-level vibration environments (from Ref. 7): (a) sinusoidal vibration, (b) random vibration**

(1) Several low-level sinusoidal sweeps at 0.46 *g* at 1 octave/min from 5 Hz to 2kHz. These sweeps were run to set initial recording gain factors, and to obtain array resonance to a constant-level base excitation input to determine amplification factors. During these runs, the array was visually observed under strobe lighting to obtain an appreciation of blanket motion. Selected channels for the low-level sweeps were analyzed for colinear and quadrature response for identification of blanket and structural modes occurring below 100 Hz. In addition, selected strain or accelerometer channels were analyzed to determine the risk of damage as the input levels were progressively increased to the qualification level.

(2) An acceptance-level sinusoidal sweep at two-thirds of the specification level was performed to evaluate the linearity of the system response, and as a final assessment of the risks associated with the full-level qualification input.

(3) The sinusoidal qualification sweep was performed with selected channel responses reviewed during preparations for subsequent random testing.

(4) Random testing followed the same sequence of low-level, acceptance-level, and qualification-level testing. Selected strain channels were evaluated as the test proceeded to assess the risk of damage during subsequent higher-level inputs.

(5) At the completion of each axis vibration test, the array structural components were visually inspected and the bi-stem actuator was operationally checked.

Table 6 lists the array resonant amplification factors and frequencies. The dynamic loads developed in the stowed vibration tests were low. Consequently, the material stresses were low, and no structural damage was experienced. The response of the array blankets was low, and the blankets provided damping for the entire system.

The following is a summary of the results of the stowed vibration tests:

(1) No significant structural modes were noted below 100 Hz.

(2) Pure blanket modes were not discovered during this test.

(3) Blanket slack was generated at the outer wraps during the course of the Y-axis (first axis of test) runs.

(4) The array structure survived the test environment in all axes. The bi-stem experienced a failure in the "fully extended" limit-switch roller actuator. In addition, a fatigue crack in the bi-stem outer rod element was discovered after the vibration test.

### E. Bi-Stem Life Demonstration Test

At the conclusion of the environmental testing program, the array was subjected to a series of 35 consecutive deployed/retract cycles under ambient conditions to demonstrate the ability of the bi-stem actuator to perform many array extensions and retractions in orbit. All of these cycles were performed without incident. At the start of this sequence, there was a relatively high fluctuation in the slip-ring apparent dynamic resistance as the drums turned. These fluctuations had the period of the drum rotation. As the number of deploy/retract cycles increased, the magnitude of these fluctuations in power slip-ring resistance decreased. This tends to indicate a wear-in period required to remove dirt or tarnish which may have collected on the rings.

## VIII. Performance During System Test Sequence

The performance of the array was monitored periodically throughout the course of the test program to check its status after each environmental test. This inspection consisted of a detailed examination of the array blankets for breakage and of the structural components for damage, the measurement of the electrical characteristics of each active solar cell module, and the deployment and retraction of the array to verify the performance of the bi-stem actuator, slip-ring assemblies, and drum bearing system. The first inspection was made after the array final assembly and established the initial condition of the test specimen prior to any environmental testing.

### A. Module Performance

From the inspections conducted during the course of this program, the maximum breakage attributable to the environmental test program has been summarized in Table 7. Several observations can be made based on these results:

(1) The stowed vibration test caused the greatest breakage of cells (0.9%) and cover glass (1.9%).

(2) The thermal vacuum test series caused the largest percentage of broken glass platelets (0.21%).

(3) The total breakage numbers indicate that the glass platelets are significantly less vulnerable to breakage than either the cells or cover glass, and that the cells are less vulnerable than the cover glass.

The fact that the thermal vacuum test was the most severe environment for the glass platelets may be explained by the fact that the areas of dummy glass were not temperature-controlled during the deploy/retract cycles and therefore were colder than the solar cell modules. Also, many localized areas of the dummy glass were affected by an overheating condition during the stowed high-temperature tests. Both of these factors could account for the disproportionate percentage of glass platelet breakage during the test. The relatively high vulnerability of the cover glass is apparent from the inspection results. There is no breakage pattern to indicate a possible cause for this high proportion of breakage, although there are a few examples of parallel, adjacent cover glasses within a module row which cracked in a direction parallel to the axis of the storage drum. Two examples of this type of cracking pattern occurred on an inboard module, which may be an indication of insufficient cushioning between the storage drum shell and the first wrap of solar cells.

### Table 5. Transducer locations and levels

| Item No. | Transducer | Station No. | Location | Run | Overall level |
|---|---|---|---|---|---|
| 1 | Microphone | D, Trk 3 | Outside +Y drum, 50% span $\theta = 0$ rad | 3 | 149.0 dB |
| 2 | Microphone | B, Trk 6 | Outside +Y drum, 50% span $\theta = \pi/2$ rad | 3 | 150.0 dB |
| 3 | Microphone | C, Trk 1 | Outside +Y drum, 0% span $\theta = 0$ rad | 3 | 150.0 dB |
| 4 | Microphone | F, Trk 4 | Outside −Y drum, 100% span $\theta = \pi$ rad | 3 | 147.5 dB |
| 5 | Microphone | A, Trk 5 | Outside −Y drum, 100% span $\theta = 3\pi/2$ rad | 3 | 150.5 dB |
| 6 | Microphone | E, Trk 2 | Inside +Y drum, 50% span on Y-axis | 3 | 151.5 dB |
| 7 | Accelerometer | 2X | LEM +Y side center couple | 3 | 7.4 g RMS |
| 8 | Accelerometer | 2Z | LEM +Y side center couple | 3 | 4.8 g RMS |
| 9 | Accelerometer | 4X | LEM 50% span +Y side | 5 | 8.0 g RMS |
| 10 | Accelerometer | 4Z | LEM 50% span +Y side | 5 | 5.5 g RMS |
| 11 | Accelerometer | 7Y | +Y end support on drum plug | 5 | 3.6 g RMS |
| 12 | Accelerometer | 11Y | +Y blanket 100% span $\theta = \pi$ rad | 3 | 5.6 g RMS |
| 13 | Accelerometer | 11Z | +Y blanket 100% span $\theta = \pi$ rad | 3 | 10.2 g RMS |
| 14 | Accelerometer | 13X | +Y drum 100% span $\theta = \pi/2$ rad | 5 | 3.3 g RMS |
| 15 | Accelerometer | 14Y | +Y drum 100% span $\theta = \pi$ rad | 5 | 2.8 g RMS |
| 16 | Accelerometer | 14Z | +Y drum 100% span $\theta = \pi$ rad | 5 | 5.2 g RMS |
| 17 | Accelerometer | 15X | +Y bearing housing | 3 | 1.5 g RMS |
| 18 | Accelerometer | 15Y | +Y bearing housing | 3 | 0.9 g RMS |
| 19 | Accelerometer | 15Z | +Y bearing housing | 3 | 1.4 g RMS |
| 20 | Accelerometer | 16X | +Y blanket 50% span $\theta = 0$ rad | 3 | 10.5 g RMS |
| 21 | Accelerometer | 18Z | +Y blanket 50% span $\theta = \pi/2$ rad | 3 | 15.6 g RMS |
| 22 | Accelerometer | 24X | +Y drum 50% span $\theta = 0$ rad | 3 | 4.0 g RMS |
| 23 | Accelerometer | 26Z | +Y drum 50% span $\theta = \pi/2$ rad | 3 | 4.9 g RMS |
| 24 | Accelerometer | 36Z | +Y blanket 0% span $\theta = 0$ rad | 3 | 6.3 g RMS |
| 25 | Accelerometer | 37Z | +Y blanket 0% span $\theta = \pi/2$ rad | 3 | 6.6 g RMS |
| 26 | Accelerometer | 38Z | +Y drum 0% span $\theta = 0$ rad | 5 | 14.3 g RMS |
| 27 | Accelerometer | 40Y | +Y drum 0% span $\theta = \pi$ rad | 5 | 2.1 g RMS |
| 28 | Accelerometer | 41Y | +Y blanket 0% span $\theta = \pi$ rad | 3 | 3.6 g RMS |
| 29 | Accelerometer | 42X | −Y blanket 50% span $\theta = 0$ rad | 3 | 10.0 g RMS |

## Table 6. Amplification factors

| Location | Station | Input and respective axis | $F_s$,[a] Hz | $A_s$[a] | $F_q$,[b] Hz | $A_q$[b] |
|---|---|---|---|---|---|---|
| Actuator at center of spool | 1 | $X$ | 125 | 2.4 | 125 | 1.6 |
| | 1 | $Y$ | 160 | 3.4 | 120 | 2.3 |
| | 1 | $Z$ | 300 | 3.9 | 300 | 2.0 |
| Center support top | 8 | $X$ | 120 | 2.1 | 120 | 1.6 |
| | 8 | $Y$ | 160 | 5.5 | 120 | 3.5 |
| | 8 | $Z$ | 160 | 3.7 | 100 | 3.8 |
| Bearing housing | 15 | $X$ | 440 | 4.2 | 440 | 3.5 |
| | 15 | $Y$ | 140 | 1.0 | 110 | 1.2 |
| | 15 | $Z$ | 350 | 4.3 | 350 | 2.1 |
| LEM at bi-stem | 2 | $X$ | 125 | 2.0 | 125 | 2.4 |
| | 2 | $Y$ | 160 | 5.7 | 125 | 4.2 |
| | 2 | $Z$ | 160 | 4.3 | 100 | 4.2 |
| LEM 50% span | 4 | $X$ | 125 | 2.2 | 130 | 1.7 |
| | 4 | $Z$ | 130 | 5.1 | 125 | 6.0 |
| LEM 75% span | 5 | $X$ | 130 | 5.1 | 130 | 1.1 |
| | 5 | $Z$ | 130 | 4.5 | 120 | 3.3 |
| Outboard drum support | 7 | $X$ | 270 | 2.4 | 270 | 2.3 |
| | 7 | $Y$ | 260 | 1.7 | 270 | 2.8 |
| | 7 | $Z$ | 280 | 1.5 | 280 | 3.8 |
| Drum | 25 | $X$ | 140 | 2.2 | No data | |
| | 40 and 28 | $Y$ | 140 | 1.5 | 110 | 1.3 |
| | 27 and 31 | $Z$ | 150 | 1.9 | 150 | 1.9 |
| Blanket | 16 | $X$ | 40 to 60 | 1.8 | 40 to 60 | 1.3 |
| | 20 | $Y$ | 30 to 80 | 1.3 to 1.9 | 10 to 16 | 2.2 |
| | 22 and 18 | $Z$ | 30 to 100 | 1.3 to 3.7 | 10 to 50 | 1.3 to 1.8 |

[a] $F_s$, $A_s$ frequency and amplification factor based on 0.46-*g* survey level excitation.

[b] $F_q$, $A_q$ frequency and amplification factors based on qualification level excitation.

**Table 7. Breakage resulting from environmental test program**

| Test environment | % broken glass platelets[a] | % broken cells[a] | % broken cover glass |
|---|---|---|---|
| Pyro shock | 0.043 | 0.025 | 0.100 |
| Thermal vacuum | 0.213 | 0.400 | 0.825 |
| Acoustic | 0.084 | 0.325 | 0.225 |
| Stowed vibration | 0.121 | 0.900 | 1.975 |
| 35 ambient deploy/retract cycles | 0.008 | 0.100 | 0.125 |
| Total breakage | 0.469 | 1.750 | 3.250 |

[a] Does not include damage known to be caused by handling and instrumentation installation and removal.

Results indicate that the cell/cover glass composite is not as resistant to damage as a corresponding 0.028-cm (0.011-in.) thick glass platelet mass simulation. The 0.0076-cm (0.003-in.) thick cover glass cracked independently of the cell in many cases. The two modules with the most cover glass breakage are located at the inboard and outboard ends of the −Y blanket, respectively. The outboard module also has the largest percentage of cell breakage. This would tend to indicate that the environment which produces breakage is more severe at both the innermost and the outermost wraps of the stowed array. It is certain that the potential for handling damage is greater on the outer wrap.

## B. Bi-Stem Performance

The bi-stem performed its function throughout the program, although some minor problems were experienced. There are three microswitches within the bi-stem actuator, which perform the following functions:

(1) Full-retract limit switch — actuated by a ramp at the top of the rod to remove power from the motor when the rod reaches the fully retracted position.

(2) Orbital retract limit switch — actuated by a roller which falls into a slot in the rod element to remove power from the motor when the rod reaches the orbital retract position [approximately 10.16 cm (4 in.) from fully retracted].

(3) Full-extend limit switch — actuated by a roller which falls into a slot in the rod element to remove power from the motor when the rod reaches the fully extended position.

At the conclusion of the testing program, none of these switches was operable. The full-retract limit switch mounting bracket was out of adjustment; it became loose during the course of the testing program. Since its function was not vital to the actuation of the bi-stem, no effort was made to repair or adjust this switch. The orbital retract limit switch roller actuator broke off during an ambient deploy/retract of the bi-stem early in the test program. The roller, which falls in the slot in the rod element, is attached to a magnesium bracket with a spring pin. This bracket is, in turn, riveted to a stainless steal leaf spring, which deflects to depress the microswitch button. The point of fracture was at the root of the bracket at the outermost rivet hole. The most probable cause of this failure is fatigue damage due to an inadequate section moment of inertia to accommodate the cyclic bending loads imposed during the component vibration test. The stress concentration at the rivet hole was probably a major contributing factor. Near the conclusion of the test program, an identical failure of the roller bracket on the full-extend limit switch was discovered when the attempt was made to deploy the bi-stem following the Z-axis stowed vibration test. This switch is located adjacent to the orbital retract limit switch and is actuated in exactly the same manner.

A fatigue crack in the bi-stem rod outer element was discovered during the preparation for the 35-cycle life demonstration following the stowed vibration test. However, no change was detected during or after the life demonstration, and the crack did not affect the function of the bi-stem. There was, however, a general increase in the noise level on the bi-stem motor current. The largest change occurred as a result of the thermal vacuum low-temperature deploy/retract cycle. It is also apparent from the test data that the time to deploy or retract at ambient conditions increased as a result of the low-temperature deploy/retract cycle. Since that increase, however, the total time to deploy or retract at ambient conditions has remained relatively constant.

## C. Slip-Ring Performance

At the beginning of the test program, the slip-ring resistance remained constant as the storage drums turned during array deployment and retraction. Some slip-ring dynamic resistance change was first recorded during the low-temperature deploy/retract cycle. Similar fluctuations, along with a slight overall increase in resistance, were recorded during the high-temperature deploy/retract cycle. The first ambient deployment following the stowed vibration test produced relatively large fluctuations in resistance, with spikes that corresponded to the period of rotation of the storage drums. After 35 ambient deploy/retract cycles, the magnitude of these fluctuations in resistance had decreased substantially. The periodic nature of the changes in resistance indicates the possibility of dirt on the power rings, which was gradually removed by the brushes as the array was deployed and retracted during the 35-cycle life demonstration.

## IX. Development Tests

During the course of the program, several subsystem or component level deployment tests were performed. The most significant are summarized below. Each test is documented in detail in the reference cited after the test title.

### A. Bi-Stem Thermal Bending Tests (Ref. 5, Section 2.3.1)

The objective of the thermal bending tests was to determine the expected solar array maximum tip deflection at a deployed length of 10.2 m (33.5 ft). The thermal vacuum chamber utilized in the investigation of boom thermal bending behavior[a] consists essentially of a vertical cylinder approximately 0.3 m (1 ft) in diameter and 3.96 m (13 ft) high. The chamber incorporates a liquid nitrogen shroud and a light source that provides an intensity equivalent to one solar constant and a uniformity of better than ±5% over the full length of a 3.05-m (10-ft) boom test specimen.

The chamber incorporates provisions for rotating the suspended test specimen relative to the fixed IR heat source. The degree of bending can be recorded photographically, as well as by optical means. Samples were removed from the test specimen for the solar absorptance measurements necessary to correct the observed bending for the differences in spectrum from the sun.

Two silver-plated 3.4-cm (1.34-in.) diameter by 3.05-m (10-ft) long bi-stem booms were evaluated. The first of these had the elements mechanically decoupled at the free end, and the second had the two elements welded together at the free end. The latter configuration more accurately represents the RA250 application, which incorporates a tip plug. The data were extrapolated to determine the maximum expected tip thermal displacement for the 10.2-m (33.5-ft) solar array boom without blanket or gravity loads. These displacements were 0.25 m (9.8 in.) and 0.34 m (13.4 in.) for the unwelded and welded configurations, respectively. When the blanket tension load is applied to the boom, the tip deflection increases by the factor

$$\delta_{\text{loaded}} = \left(1 + \frac{TL^2}{12EI}\right)\delta_{\text{unloaded}} \qquad (6)$$

where

$\delta$ = boom tip deflection, m

$T$ = total axial load on boom, N

$L$ = length of boom, m

$EI$ = section stiffness of boom, Nm$^2$

This increase amounts to about 0.05 m (2 in.) for the solar array boom. At a solar intensity of 1.5 suns, the tip deflection is 1.5 times that indicated by Eq. (6), or about 0.6 m (2 ft), assuming the tip welded data.

### B. Module Thermal Cycling Test (Ref. 5, Section 2.3.2)

Three sample solar cell modules (two 10 × 10 and one 12 × 17 cm) were thermally cycled 34 times between −128 and +140°C. The cells were interconnected with silver-expanded metal. The rear of the substrate had cushioning buttons installed as on the prototype blanket. A copper strip was also etched on the rear of the substrate to simulate the bus strip network. This copper strip was insulated with 0.0025-cm Kapton silicone pressure-sensitive tape.

Figure 23 shows the three modules mounted on the common substrate suspended in front of an array of 500-W quartz-line lamps which provide the heat input to the vacuum chamber. In addition to this active module substrate, a module of dummy glass platelets was placed in the same test, so that the thermal cycling effects on the dummy glass modules could be determined. Figure 24 shows a typical active module temperature profile during one 2500-s cycle.

A detailed visual examination of the solar cell modules revealed a failure which might be attributable to the thermal cycling test. The expanded metal interconnect strands were fractured in localized areas. This type of failure occurred only in areas where the interconnect loop had been deformed by the mesh-forming tool. Similar failures were found in formed interconnects prior to their use in assembly. The cause of this deformation was corrected by rework of the forming tool and subsequent visual inspection of each strand after forming. Thus, it is likely that the interconnect failures were not related to thermal cycling.

---

[a] Performed by NASA/Goddard Space Flight Center.

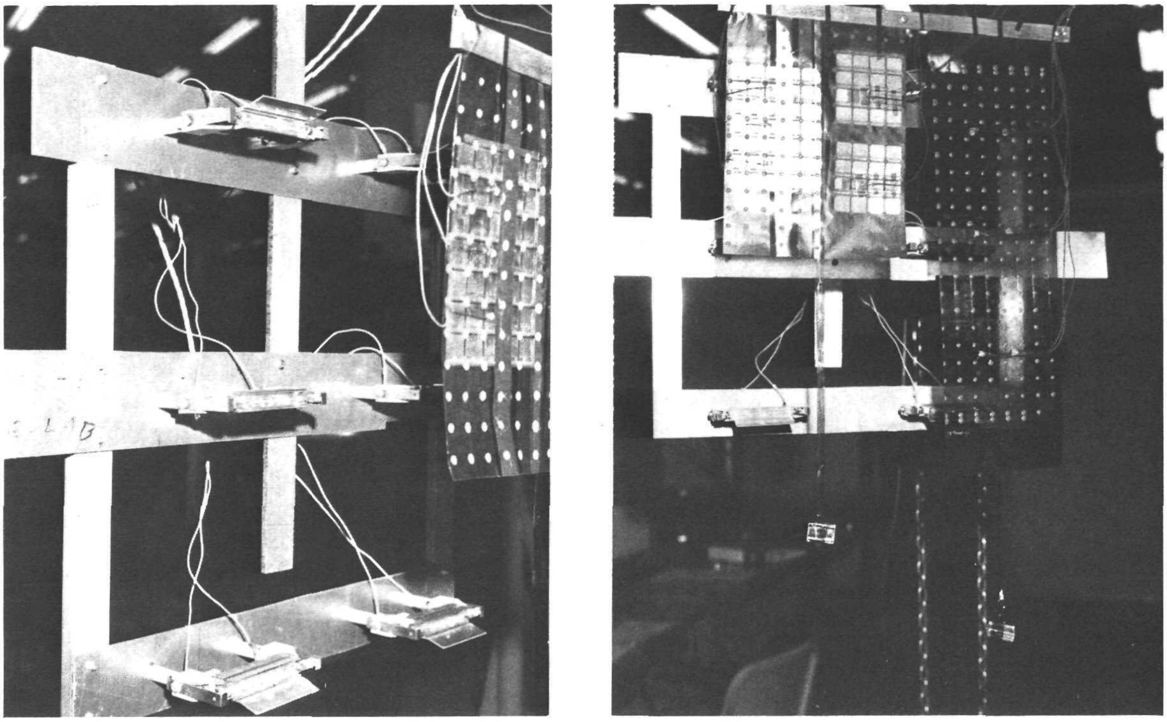

Fig. 23. Thermal cycling module test setup

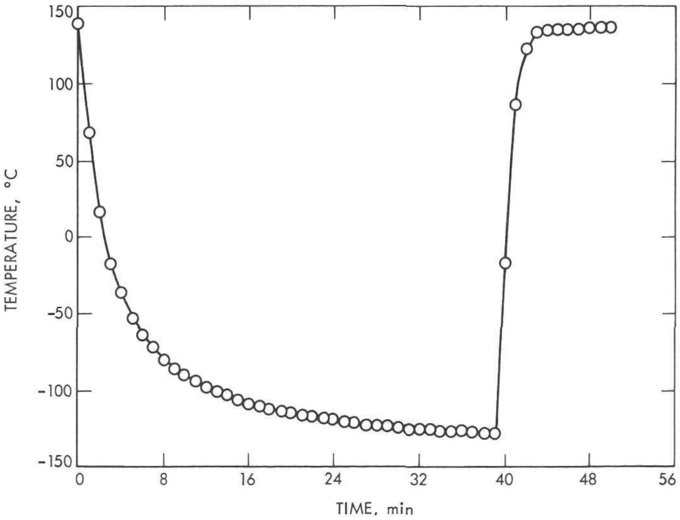

Fig. 24. Typical active module temperature profile

## C. Blanket Tracking Test (Ref. 8, Section 3.4.3)

At the completion of the 35-cycle bi-stem life demonstration, an array blanket tracking experiment was performed by displacing the array, with respect to the upward deployment aid, along the *Y* (storage drum) axis in 5.0-cm increments to check the ability to rewrap satisfactorily during retraction. At each shift increment, the array was deployed and retracted, and the blanket rewrap was observed. This procedure was continued until the total lateral displacement was 25.4 cm. During the deployment and retraction at this displacement, the inboard blanket edge on the $-Y$ side was observed to rub against the leading-edge member saddle, which is mounted on top of the bi-stem actuator. The edge guides served to redirect the rewrapping blanket, so that it restored properly on the drums. As the blanket began to ride up over the flange, it was forced to slide down the ramp of the edge guide. The major portion of the force required to produce this sliding action comes from the weight of the blanket wrap itself as it turns over the top of the storage drum. In a zero-g environment, the same sliding action would be aided by a stronger Negator spring system in the drums.

## D. Dummy Cell Module Stiffness Test (Ref. 2, Section 6.1)

The prototype subsolar array which was assembled and tested during this program had only 7% of its surface covered with active solar cells. The remaining area was covered with dummy cells. A preliminary development test was performed to determine whether the physical characteristics of the proposed construction were appreciably different from those of solar cells mounted on the typical roll-up array substrate of Kapton and cushioning buttons.

Two configurations of solar cell interconnection substitute units were assembled and evaluated for degree of stiffness simulation. Both of these dummy module configurations simulate the cell by a platelet of glass 0.033 cm thick by 3.6 cm square. The dummy interconnection for configuration 1 is the silver mesh interconnection used with solar cells, bonded to span the gap between platelets. For configuration 2, the dummy interconnection is a 0.05-mm (2-mil) strip of Kapton, the same width as the silver interconnection (0.66 cm). It is similarly bonded across the gap.

Five-by-five-cell modules were constructed for each configuration and checked for stiffness against comparable solar cell modules. The test modules included configurations 1 and 2 and a model without simulated interconnections.

Figures 25 and 26 show the deflection test setup and modules undergoing deflection testing in both the "face-up" and "face-down" directions. Both dummy configurations approximate the stiffness of the solar cell assemblies, and a wide margin separates these groups from the "glass only" module, highlighting the need for inclusion of a simulated interconnection. Kapton strips are considered to provide the best simulation of the stiffness of the solar cell modules, and these strips were incorporated into the dummy modules on the solar cell blanket for the test unit.

## E. Optimum Wrap Tension Test (Ref. 6)

During the stowed vibration test (Section VII-D), excessive slack developed in the outer wraps of the blankets when the inner wraps vibrated to a tighter wrap condition. Stability was achieved after the slack was removed by rotating the drums, but the wrap tension associated with the equilibrium condition was unknown. The goal of the wrap tension test was to establish and verify that the blankets could be wrapped initially at a tension level sufficient to prevent slack formation. This tension would be supplied externally during the initial wrapping, and would be tighter than the tension maintained in the blankets by the Negator springs in the post-launch environment.

For the test, a dc torque motor was used to supply various selected wrap tensions to the drums. The starting point was the tension required to achieve the number of blanket wraps in the previously determined stable condition. This tension level was found to be 46 N (10.4 lb), as compared with 9 N (2 lb) in the original design, but was insufficient to stabilize the stowed blanket during vibrations. This result is reasonable because the wrap conditions generated by the tension device are not the same (in detail) as the wrap condition generated during vibration testing. A tension level of 66 N (15 lb) or 0.565 N/cm (0.322 lb/in.) was found to be adequate and is the recommended value. Higher tension levels were also investigated, but they led to harsher environments. Vibration parallel to the drum axis was found to be the critical direction with respect to the generation of slack.

The amplification factor for the blanket dynamic response was found to be low (less than 3) at all tension levels and for excitation parallel and perpendicular to

Fig. 25. Face-down deflection test — active solar cell module No. 1 with 5-$g$ load

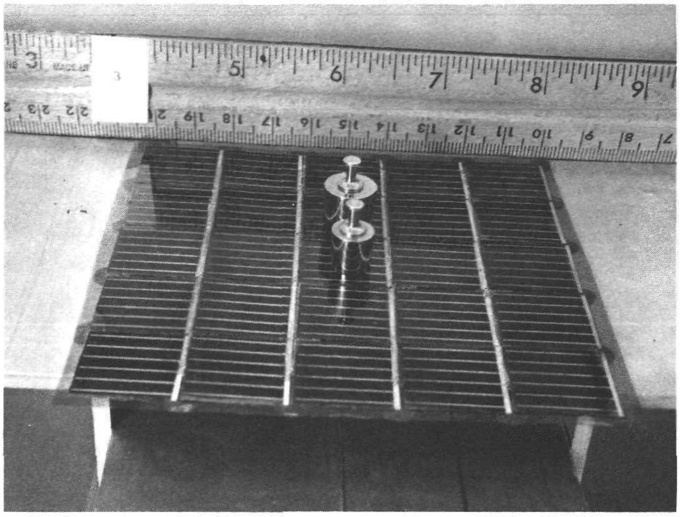

Fig. 26. Face-up deflection test — active solar cell module No. 1 with 15-$g$ load

the drum axis. Response plots, waveforms, and other data are included in detail in Ref. 6.

## X. Conclusions

The intent of the program was to design, develop, and test a lightweight solar array, and to document the results so they can be utilized for future development. Program results are given in six reports—four Quarterly Reports (Refs. 2, 3, 5, and 9), a Final Report in two volumes (Refs. 8 and 4), and a Supplemental Task Report (Ref. 6)—published as results were obtained. To help in applying these results to roll-up arrays of other sizes, a computer program was developed and a set of plots were generated that provide optimum structural sizing and estimated weights for arrays with blanket areas ranging from 9.3 to 37.2 m$^2$ (100 to 400 ft$^2$), and for first-mode natural frequencies from 0.03 to 0.7 Hz. These data are contained in Ref. 10 and may be used for a quick evaluation of the potential merits of roll-up arrays of other sizes.

The following major conclusions have been derived from the results of the program:

(1) It is possible to design a 23-m$^2$ roll-up solar array which exceeds a baseline performance of 66 W/kg for space applications. Detailed manufacturing drawings for such an array were produced, the design was verified by analysis, the weight and performance were verified by building a full-scale engineering model, and the design integrity was established by a series of environmental tests.

(2) Results of array retraction tests show that blanket tracking can be achieved by careful alignment during installation. No special control devices should be needed to aid blanket tracking during retraction.

(3) The more than 50 complete deployment/retraction cycles provide assurance that the design has a multi-cycle life capability. The life-limiting item in the design with respect to deployment/retraction cycles is considered to be the bi-stem actuator. Life tests on the bi-stem alone would provide more insight into the system deployment/retraction life capability.

(4) The array system demonstrated excellent structural integrity in severe mechanical environments (sine and random vibration, acoustic noise, and mechanical shock). The dynamic response of the solar array blanket mass was low, which resulted in low structural loads and stresses. The fact that extra runs (at least 10) of sinusoidal excitation (5 to 100 Hz) at qualification level were made without causing structural failures is an indication of the structural capability. These runs were made to observe and photograph blanket motion.

(5) The array system was shown to perform in thermal vacuum conditions, though the low-temperature retraction test results were clouded by a fouled thermocouple wire. The design margin in the Negator spring at low temperatures is small and may even be negative. The predicted thermal transients of the array blanket were verified by

test. The stowed thermal characteristics were found to be approximately as predicted, though analytical predictions and test results did not agree in all details. The integrity of the solar cell modules with silver mesh interconnects over the range of −130 to +140°C was demonstrated in a 34-cycle test.

(6) The array blanket design and fabrication process used to produce the engineering model did not yield a product that meets acceptable standards for appearance. Voids in the adhesive between cell and substrate resulted from the wrinkles inherent in the copper-clad substrate material, where the majority of the copper was etched away.

(7) New techniques for low-frequency structural dynamics testing were demonstrated. These included very-low-frequency sinusoidal excitation, slow sweep rates, a hyperbolic sweep rate for efficient testing, electro-optical methods of measuring displacements, and low-frequency vibration data analysis.

(8) The dynamic characteristics of the deployed array were measured and results compared with analysis. Excellent agreement was obtained for the lowest out-of-plane symmetric mode. Agreement for the higher out-of-plane modes was fair. The in-plane stiffness characteristics were determined experimentally, and equations were derived for the in-plane natural frequency.

(9) As a result of specific failures, the following design modifications are required for a flight design:

   (a) Redesign of the limit switch follower in the bi-stem actuator.

   (b) Specification of a different material for the sepation nut mounting flanges, if low-temperature operation is required.

   (c) Development of new blanket fabrication techniques.

(10) With respect to mechanical environment tests, it was found that the high frequency mechanical vibration environment is not representative of a spacecraft application. Even with a 272-kg vibration fixture, high-frequency excitation is not adequately transmitted from the shaker to the array structure, and certainly not to the blankets. Acoustic excitation provides the best means of inducing high frequency to the solar array blankets, though the admittance is low. Pyrotechnics provide a means of obtaining a reasonable simulation of the shock environment to be expected on a spacecraft.

(11) The test program provided some unanticipated results, including

   (a) Low dynamic response of solar cell blankets.

   (b) Blanket slack during stowed vibration.

(12) New information of general applicability to roll-up arrays in other programs includes

   (a) Bi-stem thermal deflection data.

   (b) Solar array blanket stiffness data.

   (c) Damping characteristics of deployed array.

   (d) Deployed dynamic testing techniques.

   (e) Mathematical modeling techniques for dynamic analysis of deployed arrays.

   (f) Bi-stem force/deflection data.

(13) Symmetry was assumed in the selection of sensor locations for the deployed dynamics testing. The nonsymmetry of the engineering model was sufficient to eliminate purely symmetric and antisymmetric response. If the test were to be repeated, the sensor arrangement would be modified to measure the response of both blankets and would not rely on obtaining symmetric and antisymmetric data. This experience should be factored into the test planning for future programs.

# References

1. *Feasibility Study — 30 Watts Per Pound Roll Up Solar Array Final Report,* Report No. 68SD4301, June 21, 1968. JPL Contract 951970, General Electric Company, Philadelphia, Pa.

2. *Rollup Subsolar Array,* Quarterly Report No. 2, GE-SSO-69SD4351, JPL Contract 952314, General Electric Company, Philadelphia, Pa., Sept. 15, 1969.

3. *Rollup Subsolar Array,* Quarterly Report No. 3, GE-SSO-69SD4373, JPL Contract 952314, General Electric Company, Philadelphia, Pa., Dec. 15, 1969.

4. *Rollup Subsolar Array, Volume II. Detailed Test Results,* Final Report, GE-SSO-70SD4286, JPL Contract 952314, General Electric Company, Philadelphia, Pa., Feb. 1, 1971.

5. *Rollup Subsolar Array,* Quarterly Report No. 4, GE-SSO-70SD4225, JPL Contract 952314, General Electric Company, Philadelphia, Pa., March 13, 1969.

6. *Design and Development of a Thirty Watt Per Pound 250 Square Foot Rollup Subsolar Array, Additional Tasks.* Final Report, GE-SSO-71SD4239, General Electric Company, Philadelphia, Pa., May 20, 1971.

7. *Detail Specification for 30 Watts per Pound Rollup Solar Cell Array,* Rev. E, Specification SS501407 (Internal Document), Jet Propulsion Laboratory, Pasadena, Calif., Oct. 22, 1969.

8. *Rollup Subsolar Array, Volume I. Program Summary,* Final Report, GE-SSO-70SD4286, JPL Contract 952314, General Electric Company, Philadelphia, Pa., Feb. 1, 1971.

9. *Rollup Subsolar Array,* Quarterly Report No. 1, GE-SSO-69SD4282, JPL Contract 952314, General Electric Company, Philadelphia, Pa., June 12, 1969.

10. Coyner, J.V., Jr., and Ross, R.G., Jr., Parametric Study of the Performance Characteristics and Weight Variation of Large-Area Roll-Up Solar Arrays, Technical Report 32-1502, Jet Propulsion Laboratory, Pasadena, Calif., Dec. 15, 1970.

NASA — JPL — Coml., L.A., Calif.